

## Accepted Manuscript

Title: The influence of SiO<sub>2</sub> doping on the Ni/ZrO<sub>2</sub> supported catalyst for hydrogen production through the glycerol steam reforming reaction

Authors: N.D. Charisiou, K.N. Papageridis, G. Siakavelas, V. Sebastian, S.J. Hinder, M.A. Baker, K. Polychronopoulou, M.A. Goula



PII: S0920-5861(18)30510-8  
DOI: <https://doi.org/10.1016/j.cattod.2018.04.052>  
Reference: CATTOD 11408

To appear in: *Catalysis Today*

Received date: 11-2-2018  
Revised date: 3-4-2018  
Accepted date: 24-4-2018

Please cite this article as: Charisiou ND, Papageridis KN, Siakavelas G, Sebastian V, Hinder SJ, Baker MA, Polychronopoulou K, Goula MA, The influence of SiO<sub>2</sub> doping on the Ni/ZrO<sub>2</sub> supported catalyst for hydrogen production through the glycerol steam reforming reaction, *Catalysis Today* (2018), <https://doi.org/10.1016/j.cattod.2018.04.052>

This is a PDF file of an unedited manuscript that has been accepted for publication. As a service to our customers we are providing this early version of the manuscript. The manuscript will undergo copyediting, typesetting, and review of the resulting proof before it is published in its final form. Please note that during the production process errors may be discovered which could affect the content, and all legal disclaimers that apply to the journal pertain.

## The influence of SiO<sub>2</sub> doping on the Ni/ZrO<sub>2</sub> supported catalyst for hydrogen production through the glycerol steam reforming reaction

N.D. Charisiou<sup>1,\*</sup>, K.N. Papageridis<sup>1</sup>, G. Siakavelas<sup>1</sup>, V. Sebastian<sup>2,3</sup>, S.J. Hinder<sup>4</sup>, M.A. Baker<sup>4</sup>, K. Polychronopoulou<sup>5</sup>, M.A. Goula<sup>1,\*</sup>

<sup>1</sup>Laboratory of Alternative Fuels and Environmental Catalysis (LAFEC), Department of Environmental and Pollution Control Engineering, Western Macedonia University of Applied Sciences, GR-50100, Greece

<sup>2</sup>Chemical and Environmental Engineering Department & Nanoscience Institute of Aragon (INA), University of Zaragoza, SP-50018, Zaragoza, Spain

<sup>3</sup>Networking Research Center on Bioengineering, Biomaterials and Nanomedicine, CIBERBBN, 28029 Madrid, Spain

<sup>4</sup>The Surface Analysis Laboratory, Faculty of Engineering and Physical Sciences, University of Surrey, Guildford, GU2 4DL, UK

<sup>5</sup>Department of Mechanical Engineering, Khalifa University of Science and Technology, Abu Dhabi, P.O. Box 127788, UAE

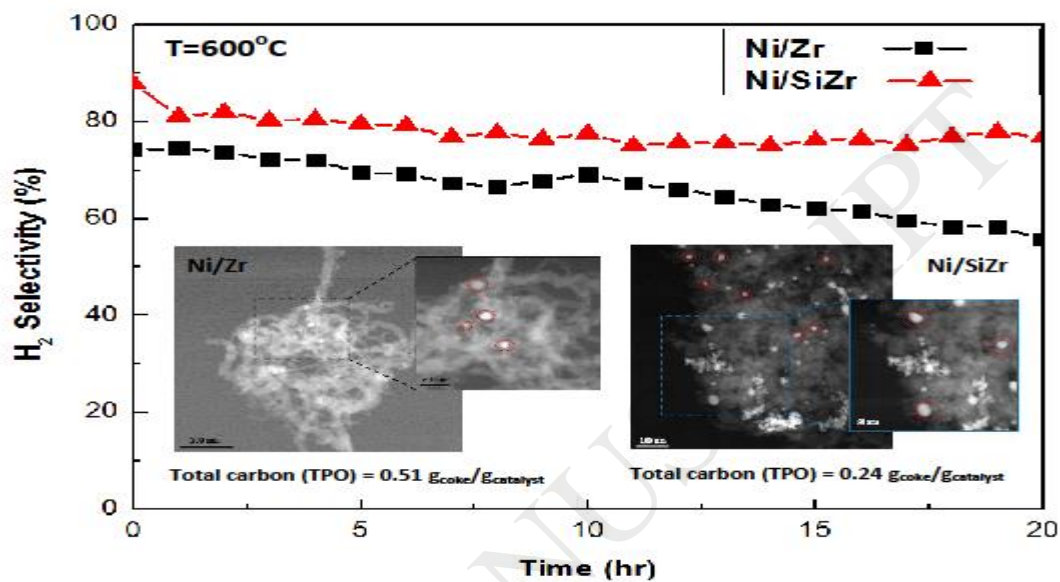
**\*Corresponding author:** Prof. Maria A. Goula

Postal Address: Western Macedonia University of Applied Sciences  
Dept. of Environmental and Pollution Control Engineering  
Lab. of Alternative Fuels and Environmental Catalysis  
Koila, Kozani, 50100, Greece

e-mail: mgoula@teiw.mg

Telephone: +30 24610 68296

## Graphical abstract



## Highlights

- SiO<sub>2</sub> stabilizes monoclinic ZrO<sub>2</sub>, restricts sintering, strengthens Ni-support interaction
- Ni/SiZr reveals increased H<sub>2</sub> yield (close to thermodynamic) and CO<sub>2</sub> selectivity
- High H<sub>2</sub>/CO ratio and a negligible CO/CO<sub>2</sub> can be achieved by the Ni/SiZr
- At 750°C acetone, acetaldehyde main products for Ni/Zr and allyl alcohol for Ni/SiZr
- Ni/SiZr (half of carbon) more resistant to deactivation in comparison with the Ni/Zr

**ABSTRACT**

The glycerol steam reforming (GSR) reaction for H<sub>2</sub> production was studied comparing the performance of Ni supported on ZrO<sub>2</sub> and SiO<sub>2</sub>-ZrO<sub>2</sub> catalysts. The surface and bulk properties were determined by ICP, BET, XRD, TPD, TPR, TPO, XPS, SEM and STEM-HAADF. It was suggested that the addition of SiO<sub>2</sub> stabilizes the ZrO<sub>2</sub> monoclinic structure, restricts the sintering of nickel particles and strengthens the interaction between Ni<sup>2+</sup> species and support. It also removes the weak acidic sites and increases the amount of the strong acidic sites, whereas it decreases the amount of the basic sites. Furthermore, it influences the gaseous products' distribution by increasing H<sub>2</sub> yield and not favouring the transformation of CO<sub>2</sub> in CO. Thus, a high H<sub>2</sub>/CO ratio can be achieved accompanying by negligible value for CO/CO<sub>2</sub>. From the liquid products quantitative analysis, it was suggested that acetone and acetaldehyde were the main products for the Ni/Zr catalyst, for 750°C, whereas for the Ni/SiZr catalyst allyl alcohol was the only liquid product for the same temperature. It was also concluded that the Ni/SiZr sample seems to be more resistant to deactivation however, for both catalysts a substantial amount of carbon exists on the catalytic surface in the shape of carbon nanotubes and amorphous carbon.

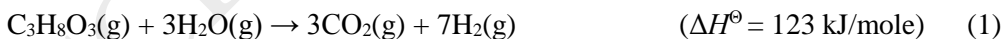
**Keywords:** Hydrogen production, glycerol steam reforming, silica-modified zirconia, nickel catalysts, carbon nanotubes, deactivation

## 1. INTRODUCTION

The reasons behind the need to move from fossil-based energy towards renewable sources are well understood and include the finite nature of the resources, issues relating to accessibility and affordability and the far reaching, long-lasting and devastating consequences that global warming will have on our planet. Biodiesel, which is derived from renewable biological sources, is increasingly gaining importance as an alternative transportation fuel [1,2]. However, the process also yields substantial amounts of crude glycerol (approximately 10 wt. % of the weight of oil undergoing the transesterification reaction is generated in glycerol), which has low commercial value and cannot be disposed directly to the environment due to its toxicity [3,4].

Nonetheless, the specific physical and chemical properties of glycerol make it an attractive platform molecule, from which a large number of high-value chemicals can be obtained, such as, ethylene glycol and propylene glycol (by hydrogenolysis) or glyceric acid and dihydroxyacetone (through selective oxidation) [5,6]. However, glycerol could also be used for the production of hydrogen, a fuel that is carbon-free and possesses the highest energy content compared to any known fuel [7,8]. Hydrogen can be produced from glycerol by catalytic reactions, such as, oxidative steam reforming (OSR) [9,10], auto-thermal reforming (ATR) [11,12], aqueous phase reforming (APR) [13,14], supercritical water (SCW) reforming [15,16] and steam reforming (GSR) [17,18].

GSR (Eq. 1), which can theoretically produce 7 moles of hydrogen per mole of glycerol, is a combination of glycerol decomposition (Eq. 2) and the water-gas shift reactions (Eq. 3). Depending on the operating conditions, it may also be accompanied by a number of possible side reactions, such as, methanation (Eq. 4), methane dry reforming (Eq. 5), methane steam reforming (Eq. 6) and a series of reactions for carbon formation (Eqs. 7-9) [19,20].



Although noble metal based catalysts are highly active and selective [e.g., 21-23] their high cost restricts their use on an industrial scale, which means that efforts focus on the use of cheaper transition metals such as Ni, Co or Cu. Nickel is known to have good intrinsic activity especially when it is highly dispersed on to the support [24-27], but systems that are based on  $\text{Al}_2\text{O}_3$  - the support most commonly used - identify as major drawbacks catalyst deactivation due to carbon deposition and metal particle sintering [28-42].  $\text{ZrO}_2$  exhibits surface acidic, basic, oxidizing and reducing properties [43], along with high thermal stability, which make it attractive as a supporting material [44]. Moreover, the properties of  $\text{ZrO}_2$ -based catalysts can be influenced by dopants [45] such as  $\text{SiO}_2$  that retards surface area loss and structure transformations, which would normally occur upon heating [46]. Since oxygen vacancies are not expected to exist in  $\text{SiO}_2$ - $\text{ZrO}_2$  catalytic systems, the observed thermal stabilization is caused by silica restricting the growth of  $\text{ZrO}_2$  particles [47,48].

Previous published works investigating the performance of Ni catalysts supported on  $\text{SiO}_2$  or  $\text{ZrO}_2$  in glycerol steam reforming are rather limited [31,49-52]. Moreover, and to the best of our knowledge, no work exists in the literature that performs an investigation of nickel catalysts based on zirconia modified with silica supporting material for the GSR. Reddy et al. [53] studied  $\text{CH}_4$  reforming with  $\text{CO}_2$  reaction under severe conditions (high temperature and space velocity) using Pt catalysts supported on  $\text{ZrO}_2/\text{SiO}_2$  mixed oxides with different ratios (2:1 to 4:1). Excellent reforming activity was observed for Pt/ $\text{ZrO}_2/\text{SiO}_2$  (4:1) sample among the various tested catalysts and was explained by higher Pt dispersion due to the absence of remaining free silica and the presence of amorphous  $\text{ZrSiO}_4$  in higher amount. Wang et al. [54] reported on CO methanation over Ni supported on  $\text{SiO}_2$  aerogel promoted with 10 wt%  $\text{ZrO}_2$  and suggested that the formation of Si-O-Zr bond results in stronger acid strength and larger amounts of acid of the  $\text{ZrO}_2$ - $\text{SiO}_2$  support. The changes of acidity lead to the increase of the interaction between NiO species and the  $\text{ZrO}_2$ - $\text{SiO}_2$  support and then enhance the dispersion degree and the reduction degree of NiO species. Thus, the Ni/ $\text{ZrO}_2$ - $\text{SiO}_2$  catalyst possesses smaller Ni crystallite size, higher Ni dispersion, more active Ni species and stronger adsorption ability for  $\text{H}_2$ , which may contribute to its higher catalytic activity for CO methanation. Zhang et al. [55] synthesized  $\text{ZrO}_2$ - $\text{SiO}_2$  mixed oxides with different Si/Zr ratio, and used these to prepare a series of Ni/ $\text{SiO}_2$ - $\text{ZrO}_2$  catalysts with different Ni loading that were tested on the HDO process using phenol and guaiacol as model compounds. The effects of Si/Zr ratio, Ni loading and reaction temperature on conversion of phenol, guaiacol and distribution of HDO products were investigated.

In a previous work by our group [56] we came to the conclusion that  $\text{ZrO}_2$  is a promising support due to its enhanced basic character and its high capability in stabilizing the nickel active phase, which leads to catalysts with strong metal-support interactions that are resistant to deactivation. Also, as  $\text{ZrO}_2$  is known to possess the ability to first adsorb and then dissociate water, it can enhance the adsorption of steam on its surface and activate the gasification of hydrocarbons in the SR and the water-gas shift reactions [57-59]. In the work presented herein we further expanded our studies in the glycerol steam reforming reaction by comparing the catalytic activity and time on stream stability of nickel catalysts (nickel loadings of 8 wt. %) based on zirconia and zirconia modified with silica. To achieve this goal the catalysts' surface and bulk properties, at their calcined, reduced and used forms, were determined by applying several characterization techniques (ICP, BET, XRD, TPD, TPR, TPO, XPS, SEM and STEM-HAADF). The catalytic performance of the catalysts was studied in order to investigate the effect of the reaction temperature on: (i) Glycerol total conversion, (ii) Glycerol conversion to gaseous products, (iii) Hydrogen selectivity and yield, (iv) Selectivity of gaseous products, (v) Selectivity of liquid products, and (vi) Molar ratio of  $\text{H}_2/\text{CO}$  and  $\text{CO}/\text{CO}_2$  in the gaseous products mixture. Notably, quantitative results of the liquid products are reported.

## **2. EXPERIMENTAL**

### **2.1 Catalyst preparation**

Commercially available pelletized zirconia (labelled Zr) and silica-zirconia (SiZr) supports were supplied by Saint Gobain NorPro; their properties are presented in Table 1. The carriers were crashed and sieved to 350-500  $\mu\text{m}$  followed by calcination at 800 °C for 4 h. The catalysts were prepared via wet impregnation of the aforementioned powders in a  $\text{Ni}(\text{NO}_3)_2 \cdot 6\text{H}_2\text{O}$  (Sigma Aldrich) aqueous solution of appropriate concentration in order to result at catalysts with a Ni loading of about 8 wt. %. After water evaporation of the slurries under continuous stirring at 75 °C for 5 h, suspensions were dried at 120 °C for 12 h and calcined in air at 800 °C for 4 h; these samples will hereafter be denoted as “calcined” catalysts. Reduced counterparts were also produced by reduction for 1 h at 800 °C in pure  $\text{H}_2$  flow; these will be hereafter denoted as “reduced” catalysts. The catalysts are labelled as Ni/Zr and Ni/SiZr.

### **2.2 Catalyst characterization**

Inductively Coupled Plasma Atomic Emission Spectroscopy (ICP-AES) was used for the determination of the total metal loading (wt. %) of the calcined catalysts. The instrument used was a Perkin-Elmer Optima 4300DV, while the detailed methodology has been described previously [42].

The 3Flex (Micromeritics, USA) accelerated surface area and porosimetry analyzer, equipped with a high-vacuum system, and three 0.1 Torr pressure transducers, was used to obtain the N<sub>2</sub> adsorption/desorption isothermal curves (recorded manometrically up to 1 bar at -196 °C). Total Specific Surface Area (SSA) was calculated by the multi-point Brunauer-Emmet-Teller (BET) method in the relative pressure range  $0.05 < p/p_0 < 0.20$ . Pore Size Distribution (PSD) was estimated by the BJH Theory. The detailed methodology followed has been described in [53].

The crystalline structure of supports and catalysts was determined by applying the X-ray diffraction (XRD) technique, using a ThermoAl diffractometer (40 kV, 30 mA, Cu K<sub>α</sub> radiation,  $\lambda = 0.154178$  nm). Diffractograms were recorded in the  $2\theta = 2-70^\circ$  range at a scanning rate of  $0.04^\circ$  over  $1.2 \text{ min}^{-1}$ . The identification of the diffraction pattern was undertaken by comparing with known structures in the International Centre for Diffraction Data database. The determination of the particle size of different phases was done using the Scherrer equation.

CO<sub>2</sub>-TPD and NH<sub>3</sub>-TPD experiments were conducted using Autochem 2920, (Micromeritics, Atlanta, USA). In particular, a gas mixture (30 NmL/min) of 5 vol.% CO<sub>2</sub>/Ar and 1 vol.% NH<sub>3</sub>/He respectively, was passed over ~0.15 g of the pre-calcined (20 vol.% O<sub>2</sub>/He, 500 °C, 2 h) using a temperature ramp of 30 °C/min, while the TCD signal was recorded continuously. Temperature programmed reduction (H<sub>2</sub>-TPR) was performed by loading 100 mg of the calcined catalysts or supports in a U-type quartz tube adapted to a continuous flow TPR/TPD apparatus coupled with mass spectrometry. A total flow of  $16 \text{ mL min}^{-1}$  was employed as feed, with a H<sub>2</sub> content of 1 % (v/v) in He. Sample temperature was varied from ambient temperature up to 950 °C, at a ramp rate of  $10 \text{ }^\circ\text{C min}^{-1}$ . The main m/z fragment registered was H<sub>2</sub>=2. Samples were pre-treated at 200 °C for 1 h under He flow and then cooled down to room temperature under the same atmosphere before the TPR spectra acquisition.

XPS analyses were performed on a ThermoFisher Scientific Instruments (East Grinstead, UK) K-Alpha+ spectrometer. XPS spectra were acquired using a monochromated Al K<sub>α</sub> X-ray source ( $h\nu = 1486.6$  eV). An X-ray spot of ~400 μm radius was employed. Survey spectra were acquired employing a Pass Energy of 200 eV. High resolution, core level spectra for all elements were acquired with a Pass Energy of 50 eV. All spectra were charge referenced against the C1s peak at 285.0 eV to correct for charging effects during acquisition. Quantitative surface chemical analyses were calculated from the high resolution, core level spectra following the removal of a non-linear (Shirley) background. The manufacturers Avantage software was used, which incorporates the appropriate sensitivity factors and corrects for the electron energy analyzer transmission function.

Scanning Electron Microscopy (SEM) was employed for the examination of the morphology of both fresh and used catalysts, using in a JEOL 6610LV. The elemental analysis was carried out by Energy Dispersive Spectroscopy (EDS) using a large area (80mm<sup>2</sup>) silicon drift detector (X-Max 80 Oxford Instruments). Images, elements maps and spectra were acquired and analyzed with the AZtech Nanoanalysis software (Oxford Instruments).

High angle annular dark field scanning transmission electron microscopy (STEM-HAADF) were performed on a Tecnai G2-F30 Field Emission Gun microscope with a super-twin lens and 0.2 nm point-to-point resolution and 0.1 nm line resolution operated at 300 kV. The HAADF detector enables the acquisition of STEM-HAADF images with atomic number contrast for high scattering angles of the electrons (Z-contrast). To prepare the samples for transmission electron microscopy studies, catalyst powder was dispersed in milli-Q water. After 30 s in an ultrasonic bath, a drop of this suspension was applied to a copper grid (200 mesh) coated with carbon film, and allowed to dry in air. To prepare the sample, the nanoparticle suspension was diluted with ethanol and sonicated for 30 s before the casting of 5  $\mu$ L on a carbon TEM grid.

The carbonaceous deposits on the spent catalysts were measured by Temperature Programmed Oxidation (TPO). For the procedure, the catalyst samples were heated linearly (10  $^{\circ}$ C min<sup>-1</sup>) from *RT* to 750  $^{\circ}$ C under 20 v/v % O<sub>2</sub>/He flow. The signals of O<sub>2</sub>, CO and CO<sub>2</sub> were continuously monitored by an MS detector (FL-9496 Balzers). Calibration of MS signals was performed with the use of self-prepared gas mixtures of known concentration.

### 2.3 Catalytic tests

The GSR was carried out in a continuous flow fixed-bed reactor at atmospheric pressure, using a set up that allowed the feeding of both liquid and gaseous streams. The system contained two vaporizers and a pre-heater (held at 350 $^{\circ}$ C to make sure that glycerol was in the gas phase) before the reactor and a condenser after it. The glycerol/ water mixture was fed to the system using an HPLC pump with a pulse dampener (the glycerol used was supplied by Sigma Aldrich and had a 99.5% purity).

Catalytic performance was assessed using two different experimental protocols. The first protocol was designed with the aim of investigating catalytic activity and selectivity at steady state conditions in the temperature range of 400-750 $^{\circ}$ C. The aqueous solution consisted of 20 % C<sub>3</sub>H<sub>8</sub>O<sub>3</sub> diluted in H<sub>2</sub>O (total liquid flow rate of 0.12 ml/min) and He. The Weight Hourly Space Velocity (WHSV) was 50,000 mL g<sup>-1</sup> h<sup>-1</sup>. Thus, the gas feed at the reactor's inlet consisted of a gas mixture of 73% H<sub>2</sub>O, 4% C<sub>3</sub>H<sub>8</sub>O<sub>3</sub> and 23% He. Following activation, the catalyst was purged with helium, while the temperature was reduced to 750 $^{\circ}$ C. Then the reaction feed was introduced

into the catalysts bed and in order to ensure operation at steady state conditions, approximately 50 minutes were spent at each step (50°C steps). This allowed obtaining three measurements for gaseous products at each temperature, helping to ensure the reproducibility of the results. Liquid products were obtained at the end of this 50 min period.

The second protocol aimed at investigating catalytic stability during time on stream experiments and in order to help provoke catalyst deactivation (and carbon deposition), more severe conditions were chosen. Thus, the glycerol concentration in the liquid stream was increased to 31 v.v. % C<sub>3</sub>H<sub>8</sub>O<sub>3</sub> (63% H<sub>2</sub>O, 7% C<sub>3</sub>H<sub>8</sub>O<sub>3</sub>, 30% He, WHSV = 50,000 mL g<sup>-1</sup> h<sup>-1</sup>). The temperature after activation was reduced at 600°C (under a flow of He), the reaction feed was introduced into the catalysts bed and measurements for gaseous products were taken at hourly intervals and for liquid products every 4 hours.

Regardless of the experimental protocol used, catalyst activation was done in situ, in a pure hydrogen flow (100 ml/min) at 800°C for 1 hr. The catalyst weight was 200 mg.

The analysis of the gaseous products was carried out on-line using a gas chromatographer (Agilent 7890A) that had two columns connected in series (HP-Plot-Q (19095-Q04, 30 m length, 0.530 mm I.D.) and HP-Molesieve (19095P-MSO, 30 m length, 0.530 mm I.D.)) and was equipped with TCD and FID detectors. The analysis of the liquid products was carried out using a combination of Gas Chromatography (Agilent 7890A, with a 5MS column, equipped with an FID detector) and Mass Spectroscopy (Agilent 5975C). Detailed information regarding liquid product analysis have been reported previously [42].

## 2.4 Reaction metrics

Catalytic performance is reported in terms of H<sub>2</sub> yield, H<sub>2</sub>, CO, CH<sub>4</sub> and CO<sub>2</sub> selectivity, glycerol conversion into gaseous products, and total glycerol conversion. The performance of the catalysts for the liquid phase products is reported in terms of acetol (C<sub>3</sub>H<sub>6</sub>O<sub>2</sub>), acetone [(CH<sub>3</sub>)<sub>2</sub>CO], allyl alcohol (CH<sub>2</sub>=CHCH<sub>2</sub>OH), acetaldehyde (C<sub>2</sub>H<sub>4</sub>O), acetic acid (C<sub>2</sub>H<sub>4</sub>O) and acrolein (C<sub>3</sub>H<sub>4</sub>O) selectivity. Performance parameters were calculated based on Equations (10)-(15):

$$\% \text{ glycerol conversion}_{(\text{global conversion})} = \left( \frac{\text{Glycerol}_{in} - \text{Glycerol}_{out}}{\text{Glycerol}_{in}} \right) \times 100 \quad (10)$$

$$\% \text{ glycerol conversion}_{(\text{gaseous products})} = \left( \frac{\text{C atoms in the gas products}}{\text{total C atoms in the feedstock}} \right) \times 100 \quad (11)$$

$$H_2 \text{ yield} = \frac{H_2 \text{ moles produced}}{\text{moles of glycerol in the feedstock}} \quad (12)$$

$$\% H_2 \text{ selectivity} = \left( \frac{H_2 \text{ moles produced}}{C \text{ atoms produced in the gas phase}} \right) \times \left( \frac{1}{RR} \right) \times 100 \quad (13)$$

where, RR is the reforming ratio (7/3), defined as the ratio of moles of H<sub>2</sub> to CO<sub>2</sub> formed.

$$\% \text{ selectivity of } i = \left( \frac{C \text{ atoms in species } i}{C \text{ atoms produced in the gas phase}} \right) \times 100 \quad (14)$$

where, species *i* refers to CO, CO<sub>2</sub> and CH<sub>4</sub>.

$$\% \text{ selectivity of } i' = \left( \frac{C \text{ atoms in species } i'}{C \text{ atoms produced in the liquid phase}} \right) \times 100 \quad (15)$$

where, species *i'* refers to acetol, acetone, allyl alcohol, acetaldehyde, acrolein and acetic acid.

### 3. RESULTS AND DISCUSSION

#### 3.1 Characterization results

##### 3.1.1 Physicochemical, structural and textural properties of catalytic samples

The ICP results indicate that the desired metal loading was achieved for both catalysts. It is noted that a nickel loadings of 8 wt. % was chosen as according to Garbarino et al. [60] for a number of oxide-supported on oxide systems, when the support is well dispersed (e.g., for alumina, zirconia, titania carriers) and loading is low with respect to the carrier surface area, impregnation procedures produce atomically dispersed species (“monolayers”), whereas above a certain loading limit, bulk supported oxide nanoparticles start to form. It has also been proposed that low nickel content helps disperse Ni particles over the catalyst surface; in contrast, at high nickel contents the surface of the catalyst’s support can be saturated with nickel, and bulk nickel oxide can be observed [17]. In fact, it was found that a 5-10 wt. % Ni loading showed the highest activity, even at lower reaction temperatures (~550 °C), while higher loading affect the performance adversely [33,40,50,61]. The decrease in glycerol conversion at higher nickel loadings is most probably due to agglomeration of nickel particles, which inhibits catalyst’s activity and stability [62]. Furthermore, Mazumder and de Lasa [63] revealed that increasing the Ni loading from 10 to 20 wt. % decreased the total basicity due to the partial blocking of support’s basic sites by the impregnated nickel species. As it was also suggested by Dieuzeide et al. [64] the Ni(II) species present on the catalysts are strongly dependent on Ni(II) loading; at high Ni(II) contents the NiO nanocrystal size increases and as a consequence the intrinsic

catalytic activity decreases. Moreover, according to Gallegos-Suárez et al. [65] the initial loading of nickel on to the catalyst can affect the average particle size of the metallic active phase during the reaction.

Table 2 presents information on the physicochemical, structural and textural properties of the calcined and reduced catalytic samples. For both samples, the drop of the specific surface area from its initial values (Table 1) to those after calcination of the support and the introduction of the Ni species (calcined samples) and the values obtained after the activation procedure (reduced samples) is similar.

The isotherm of the Ni/Zr catalyst (inset of Fig. 1) is type IV with an H4-type hysteresis which is indicative of a rather mesoporous material. This is corroborated by the pore size distribution, which shows that the majority of the population of pores is in the meso-range. In contrast, the Ni/SiZr exhibits a Type IV isotherm with an H2-type hysteresis, which is more typical of mesoporous material with some macroporosity; this is further confirmed by the corresponding pore size distribution.

The diffractogram of the calcined zirconia support (Fig. 2) showed mainly monoclinic ( $2\theta = 24.0^\circ, 28.2^\circ, 31.5^\circ, 34.4^\circ$ ) and tetragonal polymorphs ( $2\theta = 30.0^\circ, 33.9^\circ, 50.0^\circ, 59.4^\circ$  and  $62.8^\circ$ ), but after the introduction of the active species and the subsequent calcination procedure, a transformation from the monoclinic to the cubic phase ( $2\theta = 30.5^\circ, 50.5^\circ$  and  $60.4^\circ$ ) was observed. In addition, NiO was identified only on the calcined catalyst ( $2\theta = 37.2^\circ$  and  $43.2^\circ$ ) and Ni<sup>0</sup> ( $2\theta = 44.5^\circ$ ) on the reduced sample. The calcined SiZr support exhibited a more complex diffractogram and peaks of all three zirconia polymorphs, namely monoclinic ( $2\theta = 17.4^\circ, 24.0^\circ, 28.2^\circ, 31.5^\circ, 34.4^\circ, 38.5^\circ, 40.7^\circ, 44.8^\circ, 45.6^\circ, 49.2^\circ, 54.6^\circ, 55.3^\circ, 57.2^\circ, 58.0^\circ, 65.8^\circ$ ), tetragonal ( $2\theta = 30.0^\circ, 33.9^\circ, 50.0^\circ, 60.4^\circ, 62.7^\circ$ ) and cubic ( $2\theta = 30.5^\circ, 50.5^\circ, 60.4^\circ$ ) were identified. These phases were maintained even after the catalytic calcination and reduction procedures. It should be noted however that the reflections of tetragonal and cubic structures are very close and hence it is often difficult to differentiate between them [66]. Similar to the Ni/Zr sample, NiO was identified only on the calcined catalyst and Ni<sup>0</sup> on the reduced sample. The above results also suggest that addition of SiO<sub>2</sub> stabilizes the ZrO<sub>2</sub> monoclinic structure. Regarding the impact of the crystalline phase of zirconia on catalytic performance, it has been reported that tetragonal zirconia yields a higher activity in the water gas shift reaction, but a lower activity in steam reforming in comparison with monoclinic zirconia [67]. It has also been suggested that monoclinic zirconia exhibits a lower density of acid sites and a higher degree of hydration, which contributes to lower carbon formation [68].

The XRD spectra were also used to calculate the Ni<sup>0</sup> species mean crystallite size, using Scherrer analysis (Table 2). The lower value obtained after the reduction procedure for the Ni/SiZr catalyst indicates an absence of sintering. The opposite is true for the Ni/Zr catalyst, where agglomeration of Ni particles deposited on Zr is notably affecting its estimated Ni<sup>0</sup> dispersion value. This is in accordance with the literature, as it has been reported that the presence of SiO<sub>2</sub> in the support can restrict the sintering of the Ni particles [69,70]. It has also been reported that zirconia enhances the resistance of silica to steam significantly and increases the interaction between nickel and the support, and furthermore, prevents the growth of nickel oxide species during the calcination process through the formation of a ZrO<sub>2</sub>-SiO<sub>2</sub> composite structure [71].

### 3.1.2 Surface acidity-basicity estimation

The NH<sub>3</sub>-TPD profiles for the Ni/Zr and Ni/SiZr catalysts are presented in Fig. 3(a). The Ni/SiZr catalysts shows a lower peak ( $T_{\max} < 225^{\circ}\text{C}$ ) in comparison to the Ni/Zr, suggesting that the weak acid strength is decreased. Another desorption peak also appears in the range of 225-350°C, whereas the peak at around the 450°C suggests the existence of medium and strong acid sites. According to the literature [72] ZrO<sub>2</sub> is dominated from Lewis acid sites primarily due to the higher ionic character of the Zr-O bond. The doping of ZrO<sub>2</sub> with SiO<sub>2</sub> greatly increases the amount and decreases the density of acidic sites of pure ZrO<sub>2</sub> [73]. It has been also reported that the addition of low amounts SiO<sub>2</sub> in ZrO<sub>2</sub> can increase the density of acidic sites [54,74]. These findings are corroborated by the results presented herein showing that the doping of ZrO<sub>2</sub> with SiO<sub>2</sub> seems to remove the weak acidic sites and to increase the amount of the strong acidic sites.

In Fig. 3(b) the CO<sub>2</sub>-TPD profiles for the Ni/Zr and Ni/SiZr catalysts (after pre-treatment in oxygen atmosphere) are presented. A broad CO<sub>2</sub> desorption peak appeared in the case of the Ni/Zr catalyst suggesting that CO<sub>2</sub> was weakly adsorbed on the catalyst and only a kind of adsorption state was formed [75]. In the case of Ni/SiZr, the TPD profile shows at least three CO<sub>2</sub> desorption peaks: the first peak centred at lower temperature (100-200°C) can be assigned to low strength basic sites, the second peak centred at 350°C (300-450°C) can be ascribed to medium strength basic sites and the third peak centred at 600°C (500-675°C) can be ascribed to high strength basic sites. The above results are in accordance with the literature, as it has been reported that the basicity of SiO<sub>2</sub>-ZrO<sub>2</sub> is lower than that of ZrO<sub>2</sub> [76]. This is due to the fact that the surface of SiO<sub>2</sub>-ZrO<sub>2</sub> consists of low number of Zr<sup>4+</sup>-O<sup>2-</sup> acid-base centers and large amount of acidic Zr<sup>4+</sup> centers, whereas on ZrO<sub>2</sub> mainly Zr<sup>4+</sup>-O<sup>2-</sup> acid-base centers can be observed [73].

### 3.1.3 Ni species reducibility

The H<sub>2</sub>-TPR profiles of both catalysts (Fig. 4) show three broad peaks that can be ascribed to the reduction of NiO interacting with ZrO<sub>2</sub> (low and middle temperature reduction peaks) and to the reduction of NiO-ZrO<sub>2</sub> solid solutions. The Gaussian-type deconvolution shows that the reduction peak at the lowest temperature is formed by the sum of two peaks and can be associated to NiO species interacting with tetragonal ( $\approx 440^\circ\text{C}$ ) and cubic zirconia ( $\approx 500^\circ\text{C}$ ), respectively. The reduction peak at the middle temperature is formed by the sum of two peaks for the Ni/Zr catalyst (at 567 and 609°C) and one peak for the Ni/SiZr sample (614°C) and can be ascribed to NiO species bound to monoclinic zirconia [77-79]. Finally, a slight shift to higher temperatures (by about 30°C) is observed for the higher temperature reduction peaks evidenced for the Ni/SiZr catalyst, indicating a strengthening of the interaction between the nickel species and the support. It has been suggested that the reduction band at higher temperatures ( $>700^\circ\text{C}$ ) might be due to the reduction of nickel silicate species [80]. Such reduction behavior could probably be associated with silica migration resulting in NiO particles covered partially by silica islands during H<sub>2</sub> pre-treatment, as it has been reported in the literature [81].

#### 3.1.4 XPS

The XPS high-resolution spectra of Ni 2p for the Ni/Zr and Ni/SiZr catalysts are shown in Fig.5. The main Ni 2p<sub>3/2</sub> peak occurs at a binding energy of  $\approx 856$  eV for both the calcined and reduced Ni/Zr and Ni/SiZr catalysts. Considering that there are a number of possible nickel oxide/hydroxide species present with relatively similar binding energies and complex peak shapes, specific identification of the oxidised species is not possible, but the peak position and shape would suggest a mix of Ni<sup>2+</sup>/Ni<sup>3+</sup> oxides and hydroxides present at the surface [82-84] (a chemisorbed hydroxide layer typically forms on the surface of the oxide as a result of environmental exposure, as seen for both the calcined and reduced catalysts). A low binding energy shoulder corresponding to Ni<sup>0</sup> ( $\approx 853.0$  eV) can be observed for both reduced catalysts, which is absent on the calcined samples, as expected. The higher intensity Ni<sup>0</sup> peak for the Ni/Zr catalyst compared to the Ni/SiZr catalyst may indicate that the nature of the support is having an effect on the reducibility of the Ni cations, thus the ZrO<sub>2</sub> support may be enabling a greater reduction of the Ni cation species into Ni<sup>0</sup> upon calcination compared to the SiZr support.

## 3.2 Catalytic performance

### 3.2.1 Total conversion and conversion to gaseous products

Conversion of glycerol to H<sub>2</sub> by steam reforming is a combination of pyrolysis of glycerol and WGS (CO generated by pyrolysis is converted by WGS) [19]. Regardless of the operating

conditions, even in the absence of catalyst, glycerol can decompose into a mixture of  $H_2$ ,  $CO$ ,  $CO_2$ ,  $CH_4$ ,  $C_2H_4$  and  $C_2H_6$  at values close to those measured in catalytic experiments [85]. The use of catalyst, however, is found to shift the product distribution in favor of  $H_2$  and reduce the concentration of C1–C2 hydrocarbons [86]. In other words, with the absence of catalyst only the reaction of glycerol's cracking could be possible and as a result the liquids' production is higher. Thus, as with all oxygenates molecules, both thermal decomposition and catalytic reforming reactions take place during the GSR. In fact, it can be suggested that decomposition and thermal cracking reactions occur prior to entering the catalyst bed and the acid-base catalyzed reactions at the acidic and basic sites of the catalyst support [38,42,56,87].

The influence of reaction temperature ( $T$ , °C) on total glycerol conversion ( $X$  %) and glycerol conversion to gaseous products ( $X_{\text{gaseous}}$ , %) values is shown in Fig. 6. To test the reproducibility of the experimental results presented herein, the experiments concerning the Ni/Al catalyst were repeated three times and 95% confidence intervals for the mean value were calculated (results depicted in Fig. 1S). It was found that individual experimental values lay well within the corresponding confidence intervals showing a very good reproducibility of the experimental results.

An almost total conversion of glycerol (~90%) can be observed for the whole temperature range, in the case of the Ni/SiZr catalyst. On the contrary, for the Ni/Zr catalyst and the supports (Zr, SiZr) the  $X_{C_3H_8O_3}$  values started from 70-75% at low reaction temperatures (400°C) and reached 90% at the higher ones (600-750°C). As for the conversion to gaseous products, the catalytic samples seem to exhibit an almost identical performance, revealing higher values comparing to the supports for the whole reaction range temperature. Furthermore, a drastic increase to the gases production can be observed with temperature increasing from 400°C (20%) to 500°C (80%). A more gradual raising trend to the  $X_{\text{gaseous}}$  values can be seen for the supporting materials, reaching a plateau for higher reaction temperatures ( $T > 600^\circ\text{C}$ ). Interestingly, the SiZr sample seems to produce higher amount of gaseous products in comparison to the Zr one, at lower (400-450°C) and higher (500-750°C) temperatures.

The above results are in accordance with the literature, as it has been reported that an increase in temperature from 400 to 700 °C provokes an increase in the gaseous and decreases the liquid products [88]. It is also known that at low temperature the steam reforming reaction and feed's vaporization are not favoured, which causes the vast majority of the organics present in the solution to form carbonaceous deposits on the catalytic surface [89]. It has also been reported that glycerol's decomposition (taking place simultaneously with the steam reforming) involves both thermal cracking reactions prior to entering the catalyst bed and the acid-base catalyzed reactions

at the acidic and basic sites of the catalyst's supporting material [24,87]. Thus, control of metal-support interactions is essential in order to achieve a good dispersion of the active metal in the form of small nanoparticles, which can enhance the catalytically active surface. The nature of the support is also important in terms of accomplishing most adequate acid-base characteristics for the process. On the whole, it is typically the interface between metal and support, rather than the individual components themselves, which features the active region and presents new specific characteristics itself, which are different from those of the metal and the support [90].

### 3.2.2 Gaseous products selectivity

The influence of reaction temperature on H<sub>2</sub> selectivity ( $S_{H_2}$ ) and yield ( $Y_{H_2}$ ), selectivity to carbonaceous gaseous products' ( $S_{CH_4}$ ,  $S_{CO_2}$  and  $S_{CO}$ ), and H<sub>2</sub>/CO and CO/CO<sub>2</sub> molar ratios for all samples is presented in Fig. 7. As can be observed, the Ni/SiZr catalyst exhibits a higher production of H<sub>2</sub> in comparison to the Ni/Zr one for the whole temperature range, with its  $S_{H_2}$  and  $Y_{H_2}$  (Fig. 7a) taking values very close to those predicted by thermodynamics, i.e. 85% and 5.5, respectively. This improved performance can be also observed for the SiO<sub>2</sub>-ZrO<sub>2</sub> support in comparison to the pure ZrO<sub>2</sub> for the lower temperature range (400-600°C), whereas for the higher range (600-750°C) hydrogen production seems to be rather identical. However, H<sub>2</sub> production is significantly lower for the supports (50% and 3.0) in comparison to the catalytic samples.

Concerning  $S_{CO_2}$  and  $S_{CO}$  values (Fig. 7b), it can be observed that the Ni/SiZr sample is more selective towards CO<sub>2</sub> and less selective towards CO for the whole temperature range. The same observation is valid for the Ni/Zr sample but only for the lower temperature range (400-550°C), whereas for  $T > 550^\circ\text{C}$  a drastic decrease (increase) to CO<sub>2</sub> (CO) selectivity values can be observed. As for the supports, they are both more selective towards CO and less selective towards CO<sub>2</sub> for the entire range of temperature. In regards to the CH<sub>4</sub> production (Fig. 7c) both catalysts exhibit low values (~10%) for the whole temperature range. In contrast,  $S_{CH_4}$  increases with temperature for the supports with the increase more pronounced for pure ZrO<sub>2</sub>.

The influence of reaction temperature on the H<sub>2</sub>/CO and the CO/CO<sub>2</sub> molar ratios in the gaseous products' mixture can be seen in Fig. 7d. For the Ni/SiZr catalyst, the CO/CO<sub>2</sub> molar ratio is close to zero for the whole temperature range, while the H<sub>2</sub>/CO molar ratio value initially increases with temperature reaching its maximum (about 8) at 500°C; at higher temperatures it declines reaching a value of about 6 at 750°C. For the Ni/Zr catalyst, on the other side, the H<sub>2</sub>/CO ratio value descends with T, ranging between 5 and 3, whereas the CO/CO<sub>2</sub> ratio value remains lower than unity for the entire range of temperature. As for the supports, the CO/CO<sub>2</sub> ratio decreases for the lower temperatures, increases from 500 to 650°C and decreases again for

650°C < T < 750°C (it ranges from 9 to 4 for the Zr and from 5 to 3 for the SiZr). Moreover, the H<sub>2</sub>/CO molar ratio equals to unity for both supports for the higher temperatures (T > 600°C) and remains constant for the SiZr, whereas it increases with decreasing temperature (up to the value of 4) for the Zr sample.

The above findings are consistent with thermodynamic predictions, as at low reaction temperatures, a great amount of the glycerol fed forms carbon deposits, lowering the amount of gaseous products; resulting in decreasing (increasing) of the H<sub>2</sub> (CO<sub>2</sub>) concentration, respectively. [88]. With increasing temperature, thermodynamic CO selectivity increases as the WGS reaction is favoured in a back-ward direction (i.e. reverse WGS reaction is favoured), which leads to an increase in CO concentration in the products. Besides the WGS reaction, the methanation reaction is also favoured in backward direction as the reaction temperature increased, which finally leads to increased CO selectivity [91]. Additionally, at high temperatures (>650°C), the formation of CH<sub>4</sub> is inhibited due to the methane steam reforming reaction, as it has been reported for high water to glycerol feed ratios, as in our case [92].

It can be concluded that with increasing temperature, both the production of gaseous products increases and the reforming process is more favoured, helping the production of H<sub>2</sub>, whereas at temperatures higher than 500°C a high conversion to gaseous products (~80%) can be achieved with the H<sub>2</sub> content of the gas reaching its thermodynamic value (for the Ni/SiZr catalyst). It is also clear that the addition of SiO<sub>2</sub> to the ZrO<sub>2</sub> support influences the gaseous products' distribution mainly by increasing H<sub>2</sub> production and not favouring the transformation of CO<sub>2</sub> in CO, via the reverse WGS reaction. Thus, a high H<sub>2</sub>/CO ratio can be achieved accompanying by negligible value of the CO/CO<sub>2</sub> one.

### 3.2.3 Liquid products selectivity

The influence of reaction temperature on the liquid products selectivity for the catalysts and the supports is presented in Fig. 8. Acetaldehyde, acrolein, acetone, allyl alcohol, acetic acid and acetol were the main liquid products that were identified; these products were also quantified. Trace amounts of propylene glycol; 2-Cyclopenten-1-one; 2-Cyclopenten-1-one, 2-methyl; Propanoic Acid; Phenol; 2,3-Butanedione; 1,2-Ethandiol; 1,3-Dioxan-5-ol; 2-Cyclohexen-1-one; and Phenol,2-methyl were also identified. As can be seen in Fig. 8(a), acetone and acetaldehyde were the main products for the Ni/Zr catalyst, for temperature as high as 750°C; with selectivity values 61% and 39%, respectively. As for the Ni/SiZr catalyst (Fig. 8b) allyl alcohol was the only liquid product for the same temperature. In contrast the corresponding supports (Figs. 8c & 8d) produce a variety of liquid effluents even at high reaction temperatures. Specifically, for T equals

to 750°C, acetone, acetol, acetaldehyde and acetic acid were the liquid products for the Zr sample, whereas allyl alcohol and acetic acid the ones for the SiZr sample.

According to the pathway proposed by Lin [93], alcohols and carboxylic acids are intermediate compounds in the glycerol steam reforming reaction. Specifically, at low temperatures alcohols and carboxylic acids have been suggested to be the main products, whereas by increasing the temperature from 400 to 550 °C the reforming of both compounds is favoured, diminishing their proportion in the liquid phase. At temperatures of 580°C and above, 1-2 propanediol is the most abundant alcohol, while carboxylic acids are made up of acetic and propionic acids. A high increase in the proportion of 1-2 propanediol is observed as the temperature increases up to 700°C. This compound can be formed by a dehydration followed by a hydrogenation of glycerol [94]. These same tendencies are observed for the relative amount of carboxylic acids in the liquid, i.e., the proportions of acetic and propionic acids increase between 550 and 700 °C. Considering the reforming route for glycerol, acetic acid is thought to be a final compound. This increase takes place together with an increase in gas production, indicating that the temperature shifts the process towards final liquid intermediates and gaseous products [95]. Hydroxyacetone can be obtained from the dehydration of glycerol during one of the first steps in glycerol reforming. In addition, the lower the excess of water, the greater is the shift of the dehydration reactions of glycerol. These two effects might lead to a high proportion of hydroxyacetone in the condensate. At temperatures higher than 550 °C, the reforming reactions are favoured and this compound can be transformed into gases and/or other final liquid products such as alcohols, carboxylic acids and phenols [93].

It is clear from the above that the formation of condensable products is favoured at low temperatures, whereas at higher temperatures these liquid products form intermediates that lead to carbon oxides and hydrogen. According to the literature, catalysts' GSR selectivity and stability depends on a balanced distribution of basic strength [96], however this is not necessarily achieved by the use of basic materials, as acetaldehyde may also be produced via partial decomposition of 3-hydroxypropanal or through acetol formation [97,98]. Moreover, hydrogen can be produced via the dehydrogenation of the adsorbed glycerol molecules and the reaction of adsorbed organic fragments with the hydroxyl groups, which migrate from the support's surface to the active phase crystallites/support interfaces [27].

### 3.3 Catalytic stability

The time on stream results, which as explained above were undertaken at more severe conditions, are presented in Fig. 9. It can be observed (Fig. 9a) that both the Ni/Zr and Ni/SiZr catalysts

deactivate with the same slow rate, as values for glycerol total conversion drop from 80% to 65% and from 83% to 68%, and values for conversion into gaseous products drop from 45% to 39% and 49% to 38%, respectively. The variation of H<sub>2</sub> yield and selectivity with reaction time is shown in Fig. 9(b). It can be seen that H<sub>2</sub> selectivity decreases with time for both catalysts, following a sharper decline curve for the Ni/Zr (from 74% to 56%). The decline was smoother for the Ni/SiZr catalyst starting from the value of 88% and reaching the value of 77% after 20 hours. The same trend can be observed for the H<sub>2</sub> yield, with the Ni/SiZr catalyst being the more stable one with a final value of 2.1 moles H<sub>2</sub>/moles glycerol. From Fig. 9(c) it can be seen that the CO<sub>2</sub> and CO selectivity values were quite constant with reaction time for the Ni/SiZr catalyst ranging from 68% to 58% and from 30% to 40%, respectively. On the contrary, for the Ni/Zr catalyst, the S<sub>CO2</sub> and S<sub>CO</sub> reveal a variation through reaction time as the CO<sub>2</sub> selectivity decreases from 51% to 40% and the CO increases from 45% to 52%.

In Table 3 the catalytic performance of the Ni/Zr and Ni/SiZr samples described by the reaction metrics at 600 °C, at the beginning (1st measurement) and the end (after 20 h) of the time on stream experiments can be seen. As can be seen, the Ni/Zr catalyst exhibited lower values at the end of the stability testing experiments for almost all the reaction metrics, except of the CO, CH<sub>4</sub> and acetaldehyde selectivity, as well as the CO/CO<sub>2</sub> molar ratio (values of 52%, 8.2%, 16% and 1.3, respectively). As for the Ni/SiZr sample, it can be seen that after 20h time on stream it exhibits the highest value for total glycerol conversion (68%), glycerol conversion to gaseous products (38%), H<sub>2</sub> yield (2.8) and H<sub>2</sub> (77%), CO<sub>2</sub> (58%), allyl alcohol (24%), acetic acid (11%) selectivities, as well as for the H<sub>2</sub>/CO molar ratio (4.5). On the other side, it exhibits the lowest values for the CO (40%), CH<sub>4</sub> (2.3%), acetaldehyde (13%) and for the CO/CO<sub>2</sub> molar ratio (0.7). It can be concluded that Ni/SiZr catalyst seems to be more resistant to deactivation in comparison with the Ni/Zr, mainly due to its stronger-metal support interactions (TPR), confirming the high capability of silica to stabilize the active phase, most probably by preventing the sintering of metallic nickel particles during the reaction, through the formation of a SiO<sub>2</sub>-ZrO<sub>2</sub> composite structure [70,79].

### 3.4 Characterization of used catalysts

The morphology of the carbonaceous deposits on to the spent catalysts tested under experimental protocol #2 was examined using SEM (Fig. 10). This initial examination shows that carbon is evenly spread on the surface of the catalysts (carbon mapping) while tiny whiskers can be spotted on the images included herein. Fig. 11 the STEM-HAADF images obtained for the same samples (i.e., spent catalysts tested under experimental protocol #2). From the images it is clear that a

quite substantial amount of carbon exists on the catalytic surface that takes the form of crystalline carbon allotrope structures in the shape of carbon nanotubes, as well as co-existent amorphous carbon. In both cases also the encapsulated Ni particles (bright contrast) are depicted by red dashed circles.

The temperature programmed oxidation (TPO) results for the spent catalysts tested under experimental protocol #2 are presented in Fig. 12(a,b). The total amount of deposited carbon over the catalytic surface was estimated by integrating the respective TPO curves and was found about half for the Ni/SiZr sample ( $0.24 \text{ g}_{\text{coke}}/\text{g}_{\text{catalyst}}$ ) in comparison to the Ni/Zr ( $0.51 \text{ g}_{\text{coke}}/\text{g}_{\text{catalyst}}$ ), confirming that substantial coke deposition occurred during the reaction. According to the literature [99] there are at least three types of coke-derived species, currently described as (i) weakly stable amorphous  $C_{\alpha}$  ( $\text{sp}^2\text{C}$ -atoms, superficial C or graphene-like species, peak  $300\text{--}450^{\circ}\text{C}$ ), (ii)  $C_{\beta}$  (C-nanotubes, peak  $450\text{--}550^{\circ}\text{C}$ ) and (iii) stable crystalline  $C_{\gamma}$  graphite ( $\text{sp}^3\text{C}$ -atoms, peak above  $550^{\circ}\text{C}$ ) [100]. From the predominant high temperature signal seen for both spent catalysts, it could be tempting to conclude that carbon is mainly present in the form of  $C_{\gamma}$  graphite. On the other side, it is also known that such type of carbon is the most inert one and it strongly contributes to the catalyst's deactivation by encapsulating the active sites and making them no longer accessible to the reactants [101]. Having evidences of the high catalytic stability of both samples, such effect seems rather unlikely. Thus, in accordance with the literature [102-104], it could be suggested that the high temperature oxidation peak corresponds to the less toxic transitory intermediate carbon species formed during gradual transformation of reactive  $C_{\alpha}$  and/or  $C_{\beta}$  into  $C_{\gamma}$ . These species could be analogous to carbon multi wall nanotubes (MWN) previously reported to form on Ni supported catalysts [105,106], without necessarily leading to catalyst deactivation, corroborating the STEM-HAADF results presented above. It has been also proven [107-109] that supports doped with  $\text{CeO}_2$  and/or  $\text{La}_2\text{O}_3$  (as  $\text{Al}_2\text{O}_3$  or  $\text{ZrO}_3$ ) show a tendency to form less crystalline (graphitized) and more defective carbon (defects such as oxygen containing groups, cracks, dislocations, etc.). Defects introduced in the crystalline lattice of carbon are the favoured sites of attack by oxidizing gases and may help avoid the fatal encapsulation of the catalytic metal nanoparticles [110,111]. It is generally accepted that the formation of carbon species within these routes starts with formation of nickel carbide phases, either as bulk or more probably as a carbide-type shell at the surface of nickel particles [112]. Encapsulation and irreversible deactivation of the catalysts typically occurs when the rate of formation of carbon species at the surface of the carbide is higher than the diffusion or elimination rates, leading to production of irregular, mostly amorphous, carbon phases covering the nickel particles. When the

formation rate is lower, graphitic filaments occur with variable degree of order and lower problems of deactivation [113-115].

#### 4. CONCLUSIONS

In the work presented herein, the glycerol steam reforming (GSR) reaction for H<sub>2</sub> production, by comparing the performance of Ni (8 wt. %) supported on ZrO<sub>2</sub> and SiO<sub>2</sub>-ZrO<sub>2</sub> catalysts was studied. The catalysts' surface and bulk properties, at their calcined, reduced and used forms, were determined by a variety of characterization techniques such as, ICP, BET, XRD, TPD, TPR, TPO, XPS, SEM and STEM-HAADF. It was suggested that the addition of SiO<sub>2</sub> stabilizes the ZrO<sub>2</sub> monoclinic structure, restricts the sintering of the Ni particles and strengthens the interaction between the nickel species and the supporting material. Moreover, the doping of ZrO<sub>2</sub> with SiO<sub>2</sub> seems to remove the weak acidic sites, to increase the amount of the strong acidic sites and to lower the basicity.

From the catalytic testing experiments it was concluded that at temperatures higher than 500°C a high conversion to gaseous products (~80%) can be achieved; for the Ni/SiZr catalyst, the H<sub>2</sub> content of the gas reaches its thermodynamic value. It is also clear that the addition of SiO<sub>2</sub> to the ZrO<sub>2</sub> support influences the gaseous products' distribution by increasing H<sub>2</sub> production and not favouring the transformation of CO<sub>2</sub> in CO, via the reverse WGS reaction. Thus, a high H<sub>2</sub>/CO ratio can be achieved accompanying by negligible value of the CO/CO<sub>2</sub> one, providing a gaseous mixture suitable for direct feeding of fuel cells infrastructures for energy production.

From the liquid products quantitative analysis it was suggested that acetone and acetaldehyde were the main products for the Ni/Zr catalyst, for temperature as high as 750°C, whereas for the Ni/SiZr catalyst allyl alcohol was the only liquid product for the same temperature indicating a different reaction pathway. It was also concluded that Ni/SiZr catalyst seems to be more resistant to deactivation, as the total amount of deposited carbon (carbon nanotubes and co-existent amorphous carbon) was found to be about half ( $0.24 \text{ g}_{\text{coke}}/\text{g}_{\text{catalyst}}$ ) to that of the Ni/Zr ( $0.51 \text{ g}_{\text{coke}}/\text{g}_{\text{catalyst}}$ ).

#### ACKNOWLEDGEMENTS

The authors are grateful to CIBER-BBN, an initiative funded by the VI National R&D&i Plan 2008–2011, Iniciativa Ingenio 2010, Consolider Program, CIBER Actions and financed by the Instituto de Salud Carlos III (Spain) with the assistance from the European Regional

Development Fund. NDC, GS, KNP and MAG are grateful for financial support provided by the program THALIS implemented within the framework of Education and Lifelong Learning Operational Programme, co-financed by the Hellenic Ministry of Education, Lifelong Learning and Religious Affairs and the European Social Fund, Project Title: 'Production of Energy Carriers from Biomass by Products. Glycerol Reforming for the Production of Hydrogen, Hydrocarbons and Superior Alcohols'.

ACCEPTED MANUSCRIPT

## REFERENCES

1. G. Knothe, L.F. Razon, *Prog. Energy Combust. Sci.* 58 (2017) 36-59.
2. M. Guo, W. Song, J. Buhain, *Sust. Energ. Rev.* 42 (2015) 712-725.
3. D. Rua, L. Hernandez, *Int. J. Hydrogen Energ.* 41 (2016) 13811-13819.
4. C.J. Quispe, J.A. Coronado, *Renew. Sust. Energy Rev.* 27 (2013) 475-493.
5. L.M. Martinez, M. Araque, M.A. Centeno, A.C. Roger, *Catal. Today* 242 (2015) 80-90.
6. S. Bagheri, N.M. Julkapli, W.A. Yehye, *Renew. Sust. Energ. Rev.* 41 (2015) 113-127.
7. J. Ren, S. Gao, S. Tan, L. Dong, *Renew. Sust. Energy Rev.* 41 (2015) 1230-1243.
8. A. Bakenne, W. Nuttall, N. Kazantzis, *Int. J. Hydrogen Energ.* 41 (2016) 7744-7753.
9. F.D. Alvarado, F. Gracia, *Int. J. Hydrogen Energ.* 37 (2012) 14820-14830.
10. G. Yang, H. Yu, X. Huang, F. Peng, H. Wang, *Appl. Catal. B-Environ.* 127 (2012) 89-98.
11. S. Wang, X. Song, Q. Wang, G. Liu, H. Lu, *Int. J. Hydrogen Energ.* 41 (2016) 17864-17870.
12. A.L. Leal, M.A. Soria, L.M. Madeira, *Int. J. Hydrogen Energ.* 41 (2016) 2607-2620.
13. N.D. Subramanian, J. Callison, C. Richard, A. Catlow, P.P. Wells, N. Dimitratos, *Int. J. Hydrogen Energ.* 41 (2016) 18441-18450.
14. A. Seretis, P. Tsiakaras, *Renew. Energ.* 97 (2016) 373-379.
15. F.J. Gutierrez Ortiz, F.J. Campanario, P. Ollero, *Fuel* 180 (2016) 417-423.
16. F.J. Gutierrez Ortiz, F.J. Campanario, P.G. Aguilera, P. Ollero, *Energy* 96 (2016) 561-568.
17. A.Z. Senseni, F. Meshkani, M. Rezaei, *Int. J. Hydrogen Energ.* 41 (2016) 20137-20146.
18. H.N. Demsash, K.V.K. Kondamudi, A. Upadhyayula, R. Mohan, *Fuel Proc. Technol.* 169 (2018) 150-156.
19. S. Koc, A.K. Avci, *Fuel Proc. Technol.* 156 (2017) 357-365.
20. A.Z. Senseni, S.M.S. Fattahi, M. Rezaei, F. Meshkani, *Int. J. Hydrogen Energ.* 41 (2016) 10178-10192.
21. A.Z. Senseni, M. Rezaei, F. Meshkani, *Chem. Eng. Res. Des.* 123 (2017) 360-366.
22. M.A. Goula, S. Kontou, W. Zhou, X. Qin, P.E. Tsiakaras, *Ionics* 9 (2003) 248-252.
23. I.N. Buffoni, M.N. Gatti, G.F. Santori, F. Pompeo, N.N. Nichio, *Int. J. Hydrogen Energ.* 42 (2017) 12967-12977.
24. N.D. Charisiou, K.N. Papageridis, G. Siakavelas, L. Tzounis, M.A. Goula, *BioResources*, 11 (2016) 10173-10189.
25. M.A. Goula, N.D. Charisiou, P.K. Pandis, V.N. Stathopoulos, *RSC Advances*, 6 (2016) 78954-78958.
26. M. Menor, S. Sayas, A. Chica, *Fuel* 193 (2017) 351-358.

27. L.F. Bobadilla, A. Penkova, A. Alvarez, M.I. Dominguez, F. Romero-Sarria, M.A. Centeno, J.A. Odriozola, *Appl. Catal. A-Gen.* 492 (2015) 38-47.
28. I.N. Buffoni, F. Pompeo, G.F. Santori, N.N. Nichio, *Catal. Commun.* 10 (2009) 1656-1660.
29. M.A. Goula, A.A. Lemonidou, A.M. Efstathiou, *J. Catal.* 161 (1996) 626-640.
30. E.A. Sanchez, R.A. Comelli, *Int. J. Hydrogen Energ.* 39 (2014) 8650-8655.
31. A. Iriondo, J.F. Cambra, M.B. Guemez, V.L. Barrio, J. Requies, M.C. Sanchez-Sanchez, *Int. J. Hydrogen Energ.* 37 (2012) 7084-7093.
32. A. Iriondo, V.L. Barrio, J.F. Cambra, P.L. Arias, M.B. Guemez, M.C. Sanchez-Sanchez, R.M. Navarro, J.L.G. Fierro, *Int. J. Hydrogen Energ.* 35 (2010) 11622-11633.
33. E.A. Sanchez, R.A. Comelli, *Int. J. Hydrogen Energ.* 37 (2012) 14740-14746.
34. E.A. Sanchez, M.A. D'Angelo, R.A. Comelli, *Int. J. Hydrogen Energ.* 35 (2010) 5902-5907.
35. A. Ebshish, Z. Yaakob, B. Narayanan, A. Bshish, W.R.W. Daud, *Energy Proced.* 18 (2012) 552-559.
36. C.K. Cheng, S.Y. Foo, A.A. Adesina, *Catal. Today* 178 (2011) 25-33.
37. S.H. Kim, J.S. Jung, E.H. Yang, K.Y. Lee, D.J. Moon, *Catal. Today* 228 (2014) 145-151.
38. N.D. Charisiou, K.N. Papageridis, L. Tzounis, V. Sebastian, S.J. Hinder, M.A. Baker, M. AlKetbi, K. Polychronopoulou, M.A. Goula, *Int. J. Hydrogen Energ.* Article in press (<https://doi.org/10.1016/j.ijhydene.2018.02.165>).
39. N.H. Zamzuri, R. Mat, N.A.S. Amin, A. Talebian-Kiakalaieh, *Int. J. Hydrogen Energ.* 42 (2017) 9087-9098.
40. H.D. Demsash, R. Mohan, *Int. J. Hydrogen Energ.* 41 (2016) 22732-22742.
41. A. Iriondo, V.L. Barrio, J.F. Cambra, P.L. Arias, M.B. Guemez, R.M. Navarro, M.C. Sanchez-Sanchez, J.L.G. Fierro, *Top. Catal.* 49 (2008) 46-58.
42. M.A. Goula, N.D. Charisiou, K.N. Papageridis, G. Siakavelas, *Chin. J. Catal.*, 37 (2016), 1949-1965.
43. K. Tanabe, *Mater. Chem. Phys.* 13 (1985) 347-364.
44. K.T. Jung, A.T. Bell, *J. Mol. Catal. A Chem.* 163 (2000) 27-42.
45. R. Nielsen, *Ullmann's Encyclopedia of Industrial Chemistry*, seventh ed., Wiley-VCH, 2007.
46. J.B. Miller, S.E. Rankin, E.I. Ko, *J. Catal.* 148 (1994) 673-682.
47. F. Del Monte, W. Larsen, J.D. Mackenzie, *J. Am. Ceram. Soc.* 83 (2000) 628-634.
48. F. Del Monte, W. Larsen, J.D. Mackenzie, *J. Am. Ceram. Soc.* 83 (2000) 1506-1512.
49. F. Pompeo, G.F. Santori, N.N. Nichio, *Catal. Today* 172 (2011) 183-188.

50. V. Nichele, M. Signoretto, F. Menegazzo, A. Gallo, V.D. Santo, G. Cruciani, G. Cerrato, *Appl. Catal. B-Environ.* 111-112 (2012) 225-232.
51. I. Rossetti, A. Gallo, V. dal Santo, C.L. Bianchi, V. Nichele, M. Signoretto, E. Finocchio, G. Ramis, A. di Michele, *ChemCatChem.* 5 (2013) 294-306.
52. G. Sadanandam, N. Sreelatha, M.V.P. Sharma, S.K. Reddy, B. Srinivas, K. Venkateswarlu, T. Krishnudu, M. Subrahmanyam, V.D. Kumari, *ISRN Chem. Eng.* Article ID 591587 (2012) 10 pages.
53. G.K. Reddy, S. Loridant, A. Takahashi, P. Delichere, B.M. Reddy, *Appl. Catal. A-Gen.* 389 (2010) 92-100.
54. Y. Wang, R. Wu, Y. Zhao, *Catal. Today* 158 (2010) 470-474.
55. X. Zhang, T. Wang, L. Ma, Q. Zhang, X. Huang, Y. Yu, *Appl. Energ.* 112 (2013) 533-538
56. N.D. Charisiou, K.N. Papageridis, G. Siakavelas, L. Tzounis, K. Kousi, M.A. Baker, S.J. Hinder, V. Sebastian, K. Polychronopoulou, M.A. Goula, *Top. Catal.* 60 (2016) 1226-1250.
57. M.H. Youn, J.G. Seo, H. Lee, Y. Bang, J.S. Chung, I.K. Song, *Appl. Catal. B-Environ.* 98 (2010) 57-64.
58. K.G. Azzam, I.V. Babich, K. Seshan, L. Lefferts, *J. Catal.* 251 (2007) 153-162.
59. I. Rossetti, J. Lasso, V. Nichele, M. Signoretto, E. Finocchio, G. Ramis, A. di Michele, *Appl. Catal. B-Environ.* 150-151 (2014) 257-267.
60. G. Garbarino, S. Chitsazan, T.K. Phung, P. Riani, G. Busca, *Appl. Catal. A-Gen.* 505 (2015) 86-97.
61. Y. Choi, N.D. Kim, J. Baek, W. Kim, H.J. Lee, J. Yi, *Int. J. Hydrogen Energ.* 36 (2011) 3844-3852.
62. S. Bepari, N.C. Pradhan, A.K. Dalai, *Catal. Today* 291 (2017) 36-46.
63. J. Mazumder, de H. Lasa, *Appl. Catal. B-Environ* 160-161 (2014) 67-79
64. M.L. Dieuzeide, M. Jobbagy, N. Amadeo, *Int. J. Hydrogen Energ.* 39 (2014) 16976 – 16982.
65. E. Gallegos-Suárez, A. Guerrero-Ruiz, M. Fernández-García, I. Rodríguez-Ramos, A. Kubacka, *Appl. Catal. B-Environ.* 165 (2015) 139-148.
66. C. Melchor-Hernández, A. Gomez-Cortes, G. Díaz, *Fuel* 107 (2013) 828-835.
67. S. Li, M. Li, C. Zhang, S. Wang, X. Ma, J. Gong, *Int. J. Hydrogen Energ.* 37 (2012) 2940-2949.
68. E.B. Silveira, R.C. Rabelo-Neto, F.B. Noronha, *Catal. Today* 289 (2017) 289-301.

69. V. Shanmugam, R. Zapf, S. Neuberg, V. Hessel, G. Kolba, *Appl. Catal. B-Environ.* 203 (2017) 859-869.
70. X. Xiang, H. Zhao, J. Yang, J. Zhao, L. Yan, H. Song, L. Chou, *Appl. Catal. A-Gen.* 520 (2016) 140-150.
71. J.G. Seo, M.H. Youn, I.K. Song, *J. Power Sources* 168 (2007) 251-257.
72. S. Damyanova, P. Grange, B. Delmon, *J. Catal.* 168 (1997) 421-430.
73. T. Viinikainen, H. Ronkkonen, H. Bradshaw, H. Stephenson, S. Airaksinen, M. Reinikainen, P. Simell, O. Krause, *Appl. Catal. A-Gen.* 362 (2009) 169-177.
74. J.A. Anderson, C. Fergusson, I. Rodriguez-Ramos, A. Guerrero-Ruiz, *J. Catal.* 192 (2000) 344-354.
75. L. Qian, Z.F. Yan, *Fuel Chemistry Division Preprints* 47 (2002) 598-602.
76. Z. Dang, B.G. Anderson, Y. Amenomiya, B.A. Morrow, *J. Phys. Chem.* 99 (1995) 14437-14443.
77. Y. Li, D. He, Q. Zhu, X. Zhang, B. Xu, *J. Catal.* 221 (2004) 584-593.
78. M.H. Youn, J.G. Seo, J.C. Jung, S. Park, D.R. Park, S.-B. Lee, *Catal. Today* 146 (2009) 57-62.
79. H. Teterycz, R. Klimkiewicz, M. Łaniecki, *Appl. Catal. A-Gen.* 249 (2003) 313-326.
80. G.S. Jeong, M.H. Youn, I.K. Song, *J. Power Sources* 168 (2007) 251-257.
81. D. Liu, Y. Wang, D. Shi, X. Jia, X. Wang, A. Borgna, R. Lau, Y. Yang, *Int. J. Hydrogen Energ.* 37 (2012) 10135-10144.
82. A.P. Grosvenor, M.C. Biesinger, R.St.C. Smart, N.S. McIntyre, *Surf. Sci.* 600 (2006) 1771-1779.
83. K.T. Tung, D.M. Hercules, *J. Phys. Chem.* 80 (1976) 2094-2012.
84. K.S. Kim, N. Winograd, *Surf. Sci.* 43 (1974) 625-643.
85. V. Chiodo, S. Freni, A. Galvagno, N. Mondello, F. Frusteri, *Appl. Catal. A-Gen.* 381 (2010) 1-7.
86. L. Bobadilla, A. Álvarez, M. Domínguez, F. Romero-Sarria, M. Centeno, M. Montes, J. Odriozola, *Appl. Catal. B-Environ.* 123 (2012) 379-390.
87. L.F. Bobadilla, A. Penkova, F. Romero-Sarria, M.A. Centeno, J.A. Odriozola, *Int. J. Hydrogen Energ.* 39 (2014) 5704-5712.
88. J. Remón, C. Jarauta-Córdoba, L. García, J. Arauzo, *Fuel Process. Technol.* 145 (2016) 130-147.
89. J.M. Silva, M.A. Soria, L.M. Madeira, *Renew. Sust. Energ. Rev.* 42 (2015) 1187-1213.

90. A. Kubacka, M. Fernández-García, A. Martínez-Arias, *Appl. Catal. A-Gen.* 518 (2016) 2-17.
91. D.D. Chirag, K.K. Pant, *Renew. Energ.* 36 (2011) 3195-3202.
92. Y. Li, W. Wang, B. Chen, Y. Cao, *Int. J. Hydrogen Energ.* 35 (2010) 7768-7777.
93. Y.-C. Lin, *Int. J. Hydrogen Energ.* 38 (2013) 2678-2700.
94. Z. Yuan, J. Wang, L. Wang, W. Xie, P. Chen, Z. Hou, X. Zheng, *Bioresour. Technol.* 101 (2010) 7099-7103.
95. A. Wawrzetz, B. Peng, A. Hrabar, A. Jentys, A.A. Lemonidou, J.A. Lercher, *J. Catal.* 269 (2010) 411-420.
96. D. Stosic, S. Bennici, S. Sirotin, C. Calais, J.L. Couturier, J.L. Dubois, A. Travert, A. Auroux, *Appl. Catal. A-Gen.* 447-448 (2012) 124-134.
97. E. Tsukuda, S. Sato, R. Takahashi, T. Sodesawa, *Catal. Commun.* 8 (2007) 1349-1353.
98. K. Pathak, K.M. Reddy, N.N. Bakhshi, A.K. Dalai, *Appl. Catal. A-Gen.* 372 (2010) 224-238.
99. K. Jabbour, P. Massiani, A. Davidson, S. Casale, N. El Hassan, *Appl. Catal. B-Environ.* 201 (2017) 527-542.
100. J.Z. Luo, Z.L. Yu, C.F. Ng, C.T. Au, *J. Catal.* 194 (2000) 198-210.
101. J. Guo, H. Lou, X.M. Zheng, *Carbon* 45 (2007) 1314-1321.
102. Z.L. Zhang, X.E. Verykios, *Catal. Today* 21 (1994) 589-595.
103. M.D. Argyle, C.H. Bartholomew, *Catalysts* 5 (2015) 145-269.
104. L. Zhou, L. Li, N. Wei, J. Li, J.M. Basset, *ChemCatChem.* 16 (2015) 2508-2516.
105. K.N. Papageridis, N.D. Charisiou, G. Siakavelas, D.G. Avraam, L. Tzounis, K. Kousi, M.A. Goula, *Fuel Proc. Technol.* 152 (2016) 156-175.
106. N.D. Charisiou, G. Siakavelas, K.N. Papageridis, A. Baklavaridis, L. Tzounis, K. Polychronopoulou, M.A. Goula, *Int. J. Hydrogen Energ.* 42 (2017) 13039-13060.
107. M.A. Goula, N.D. Charisiou, K.N. Papageridis, A. Delimitis, E. Pachatouridou, E.F. Iliopoulou, *Int. J. Hydrogen Energ.* 40 (2015) 9183-9200.
108. N.D. Charisiou, G. Siakavelas, K.N. Papageridis, A. Baklavaridis, L. Tzounis, D.G. Avraam, M.A. Goula, *J. Natural Gas Sci. Eng.* 31 (2016) 164-183.
109. M.A. Goula, N.D. Charisiou, G. Siakavelas, L. Tzounis, I. Tsiaoussis, P. Panagiotopoulou, G. Goula, I.V. Yentekakis, *Int. J. Hydrogen Energ.* 42 (2017) 13724-13740.
110. M. Velasquez, C. Batiot-Dupeyrat, J. Gallego, A. Santamaria, *Diam. Relat. Mater.* 50 (2014) 38-48.
111. K.P. de Jong, J.W. Geus, *Catal. Rev. Sci. Eng.* 42 (2000) 481-490.

112. D.A. Gómez-Gualdrón, J.M. Beetge, P.B. Balbuena, J. Phys. Chem. C 117 (2013) 12061-12070.
113. V.C. Kroll, H.M. Swaan, C. Mirodatos, J. Catal. 161 (1996) 409-422.
114. J.H. Kim, D.J. Suth, T.J. Park, Appl. Catal. A-Gen. 197 (2000) 191-200.
115. S. Tang, L. Ji, J. Lin, H.C. Zeng, K.L. Tang, K. Li, J. Catal. 194 (2000) 424-430.

ACCEPTED MANUSCRIPT

**Figures captions**

**Fig 1.** Pore size distribution and N<sub>2</sub> adsorption-desorption isotherms (inset) of the reduced catalysts.

**Fig 2.** XRD patterns of the supports and calcined and reduced catalysts (a) Zr and Ni/Zr, and (b) SiZr and Ni/SiZr.

**Fig 3.** (a) NH<sub>3</sub>-TPD and (b) CO<sub>2</sub>-TPD profiles of the Ni/Zr and Ni/SiZr catalysts.

**Fig 4.** TPR profiles of Ni/Zr and Ni/SiZr catalysts.

**Fig 5.** XPS spectra for Ni/Zr and Ni/SiZr calcined and reduced catalytic samples.

**Fig 6.** Total glycerol conversion and glycerol conversion into gaseous products for all samples [Results obtained for samples tested under experimental protocol #1].

**Fig 7.** (a) H<sub>2</sub> selectivity and H<sub>2</sub> yield, (b) CO<sub>2</sub>, CO selectivity, (c) CH<sub>4</sub> selectivity, and (d) H<sub>2</sub>/CO and CO/CO<sub>2</sub> molar ratio [Results obtained for samples tested under experimental protocol #1].

**Fig 8.** Liquid products selectivity for the supports and catalysts tested herein [Results obtained for samples tested under experimental protocol #1].

**Fig 9.** Time on stream experiments for the Ni/Zr and Ni/SiZr catalysts: (a) Total glycerol conversion and glycerol conversion into gaseous products, (b) H<sub>2</sub> selectivity and H<sub>2</sub> yield, and (c) CO<sub>2</sub>, CO and CH<sub>4</sub> selectivity [Results obtained for samples tested under experimental protocol #2].

**Fig 10.** SEM images and carbon mapping of the spent catalysts: (a) Ni/Zr, and (b) Ni/SiZr [Results obtained for samples tested under experimental protocol #2].

**Fig 11.** STEM-HAADF images of: (a) Ni/Zr, and (b) Ni/SiZr catalysts [Results obtained for samples tested under experimental protocol #2].

**Fig 12.** TPO profiles and total amount of deposited carbon obtained for the spent catalytic samples [Results obtained for samples tested under experimental protocol #2].

ACCEPTED MANUSCRIPT

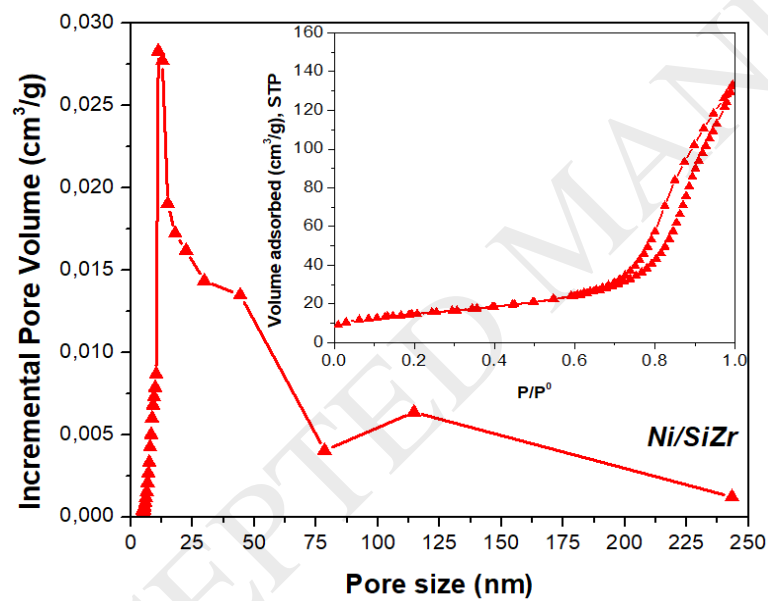
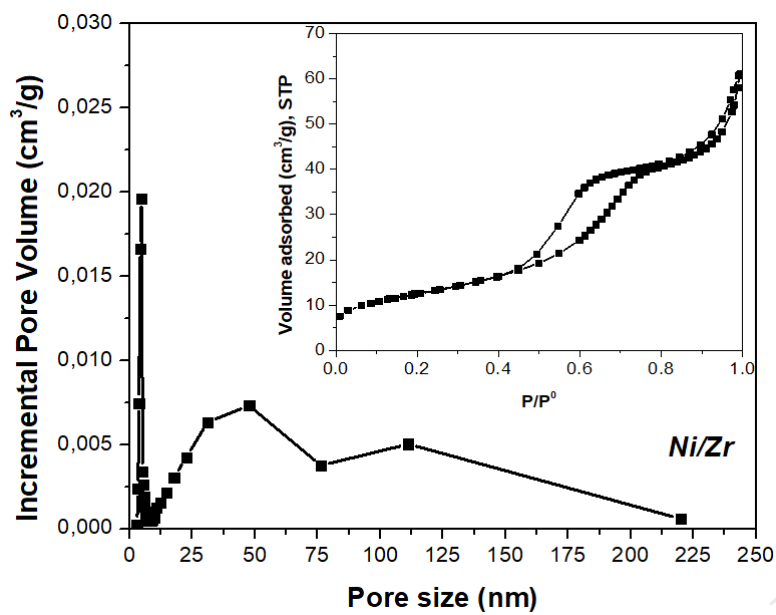


Fig 1.

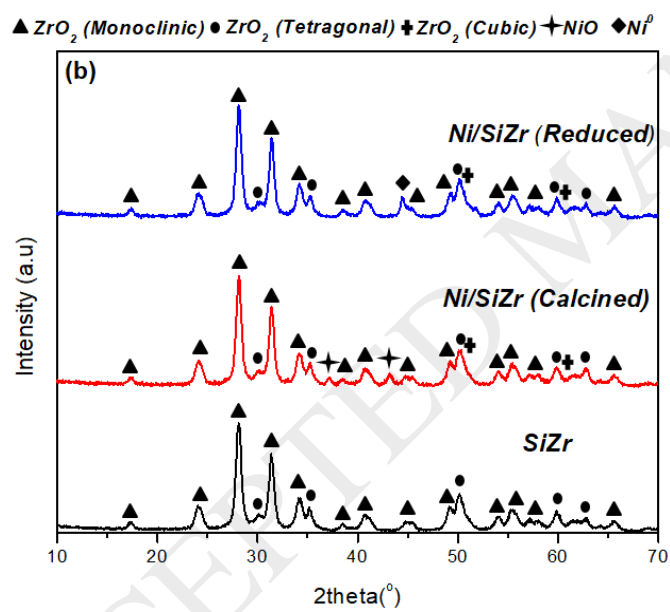
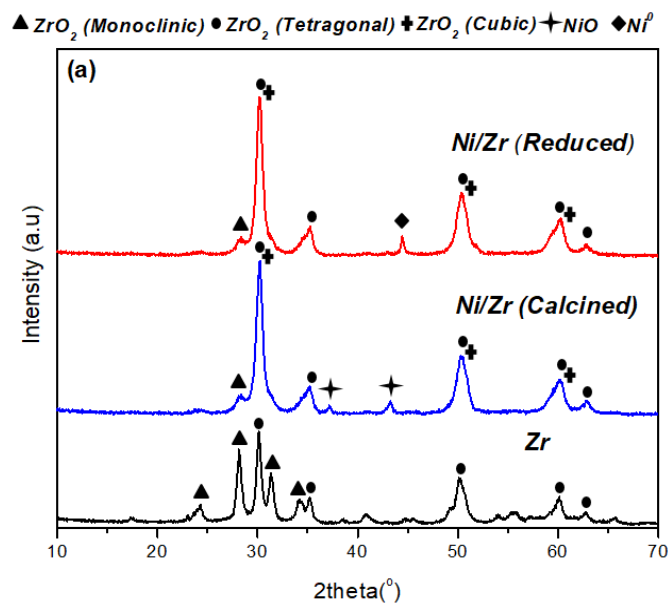


Fig 2.

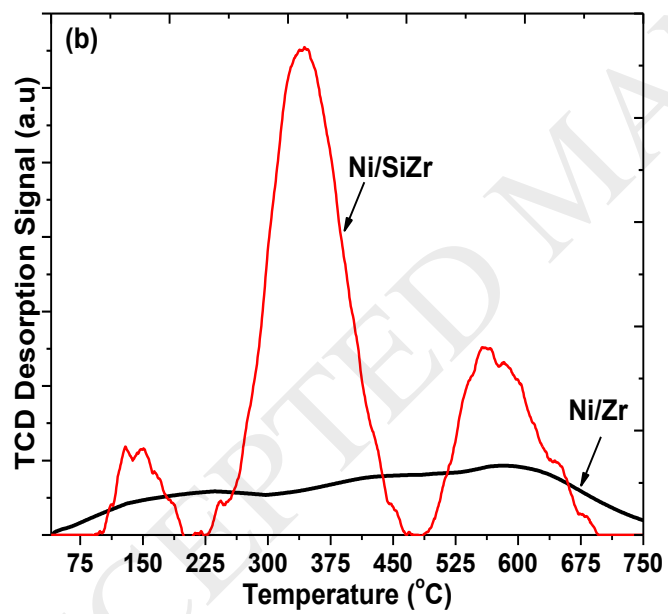
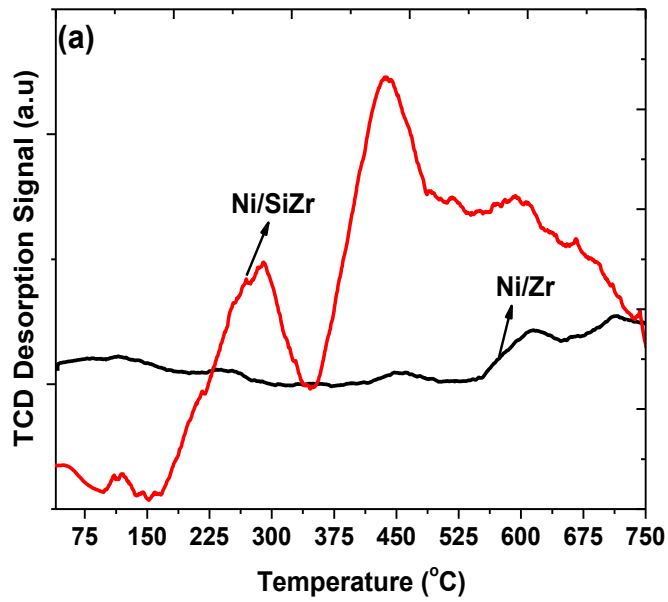


Fig 3.

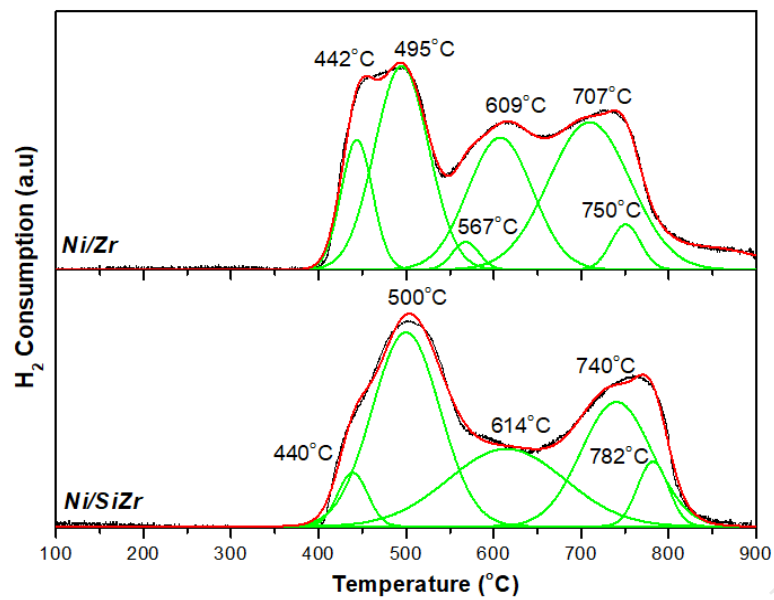


Fig 4.

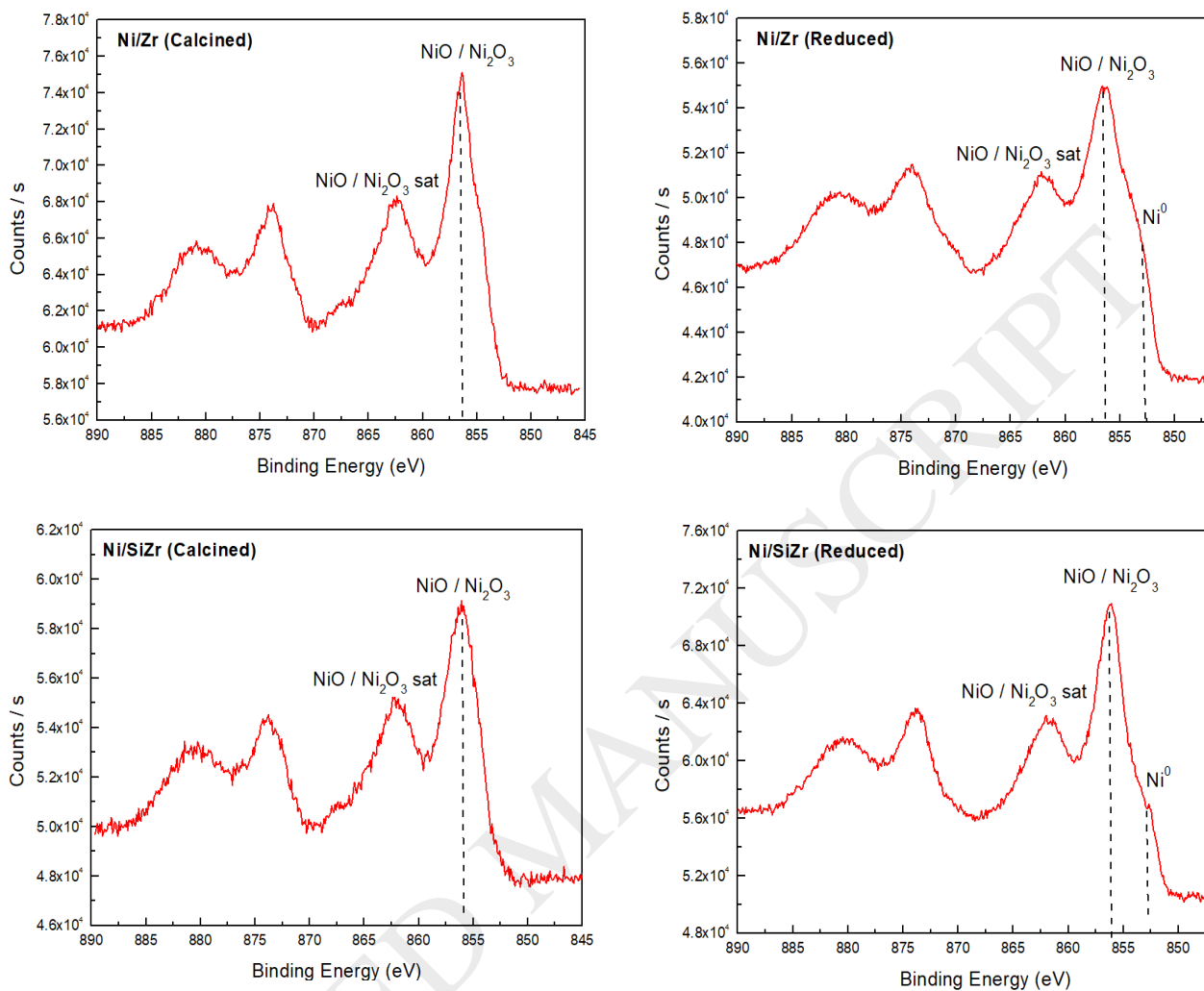


Fig 5.

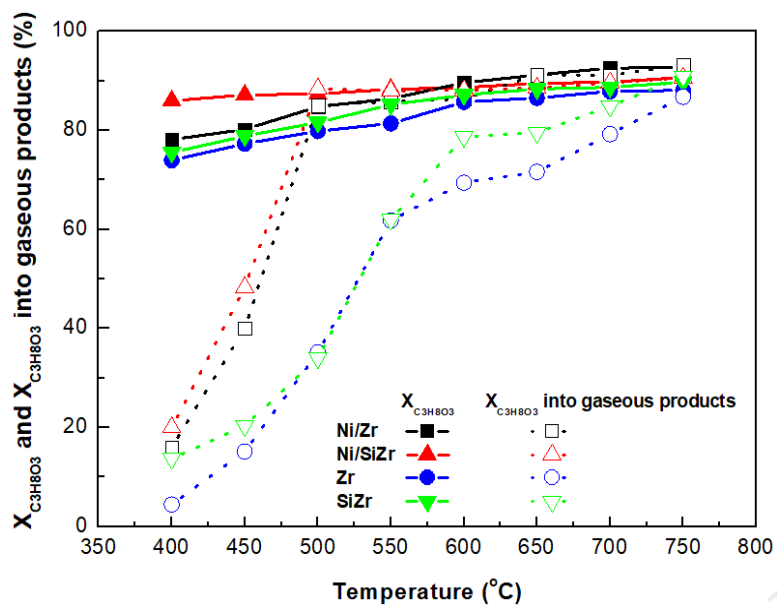


Fig 6.

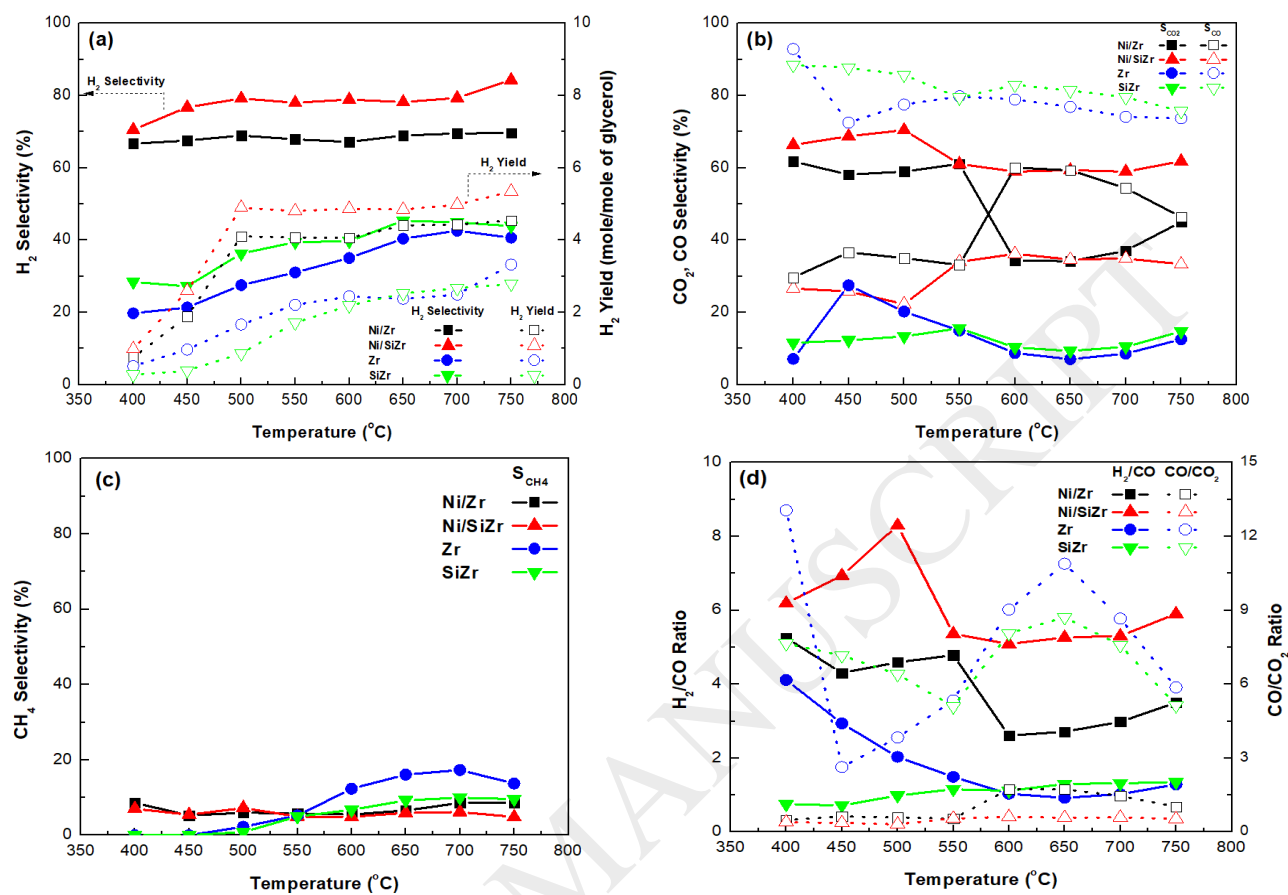


Fig 7.

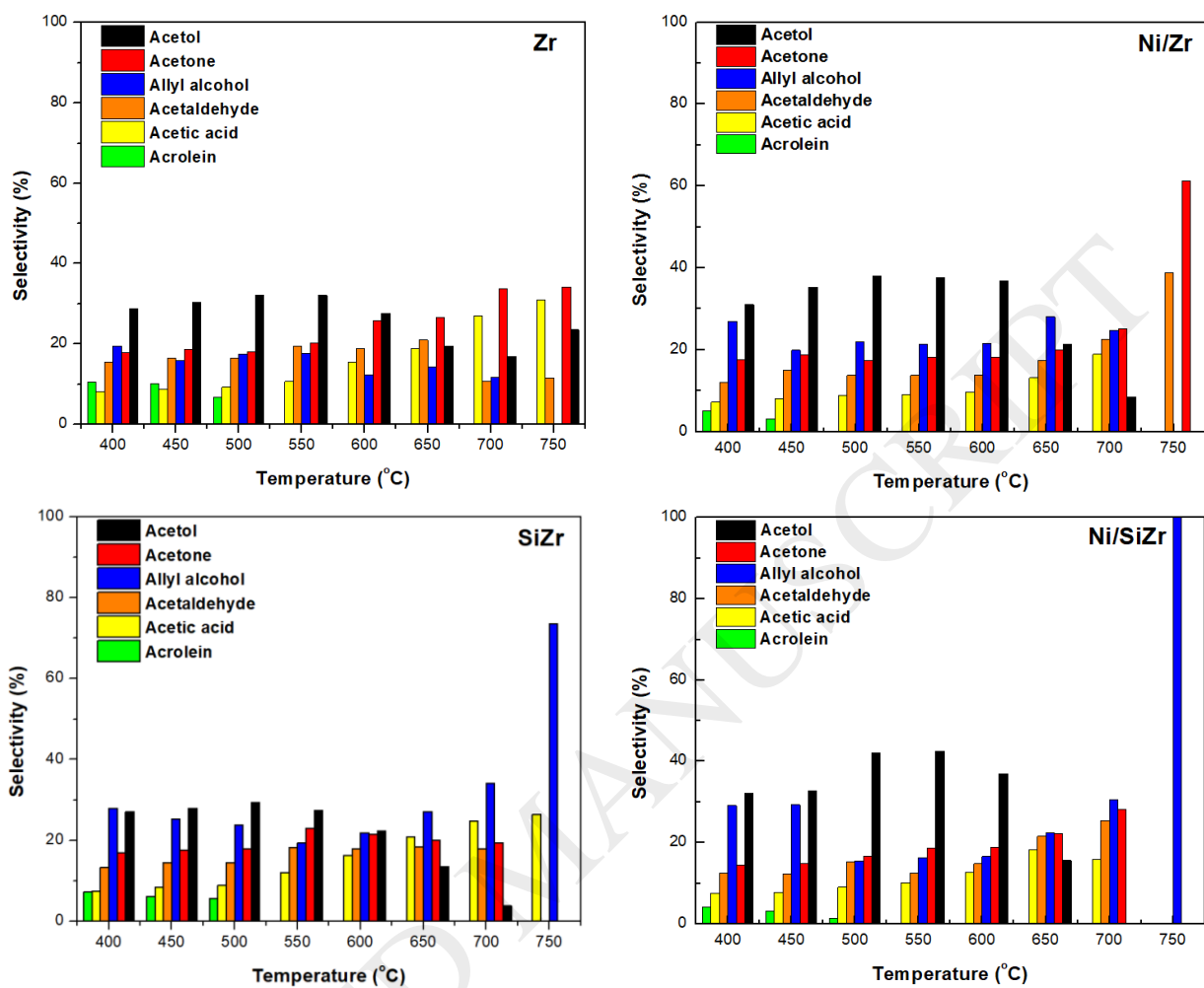


Fig 8.

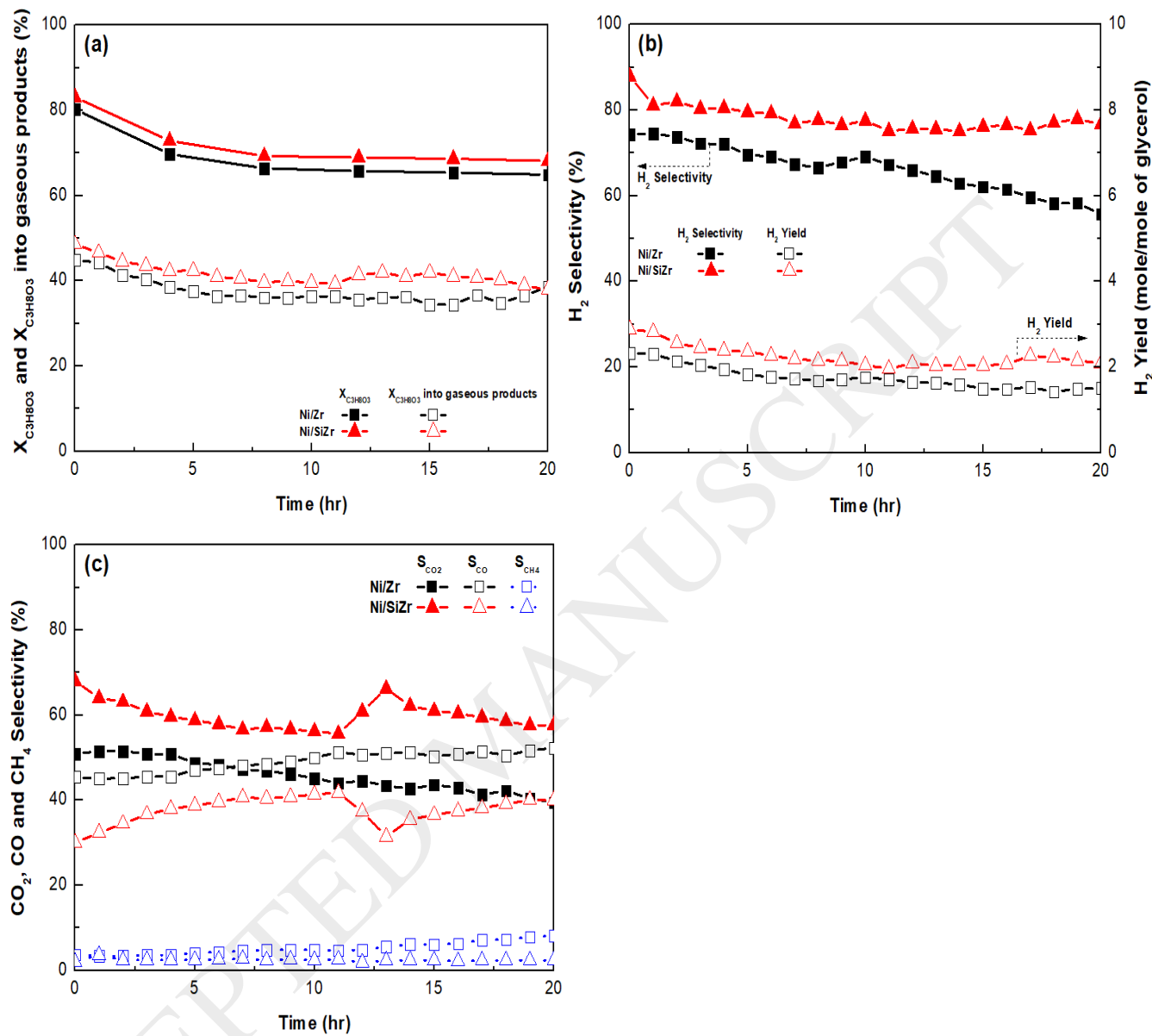
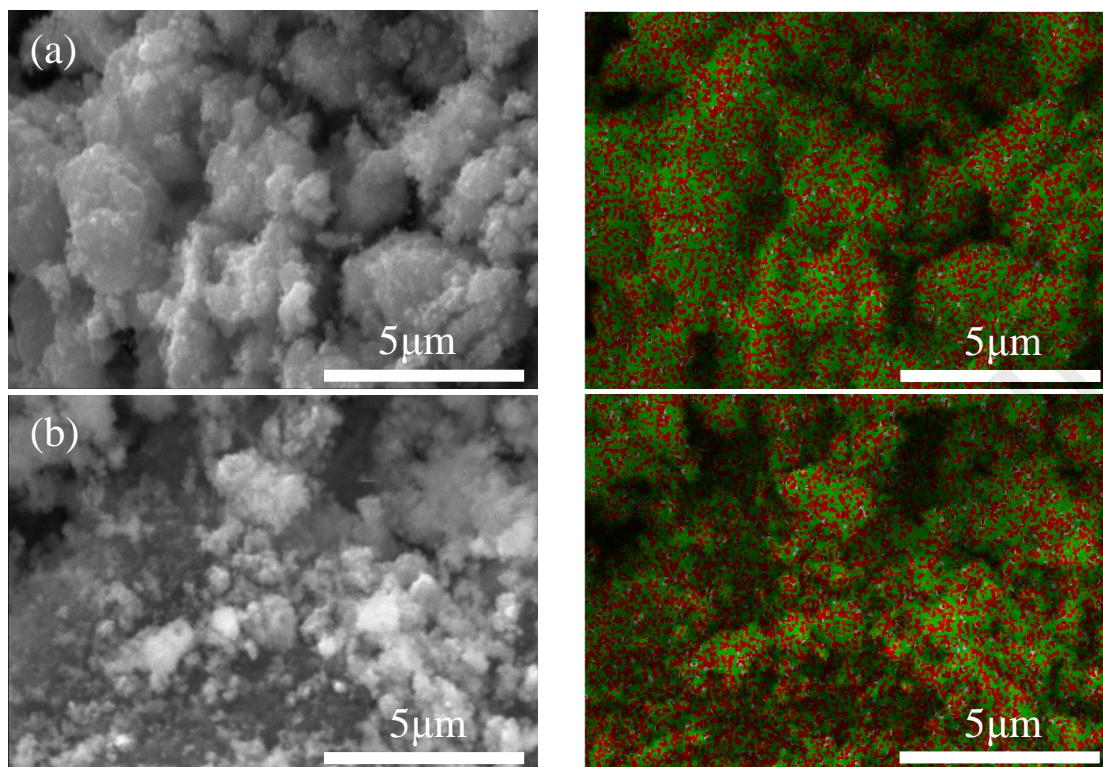


Fig 9.



**Fig 10.**

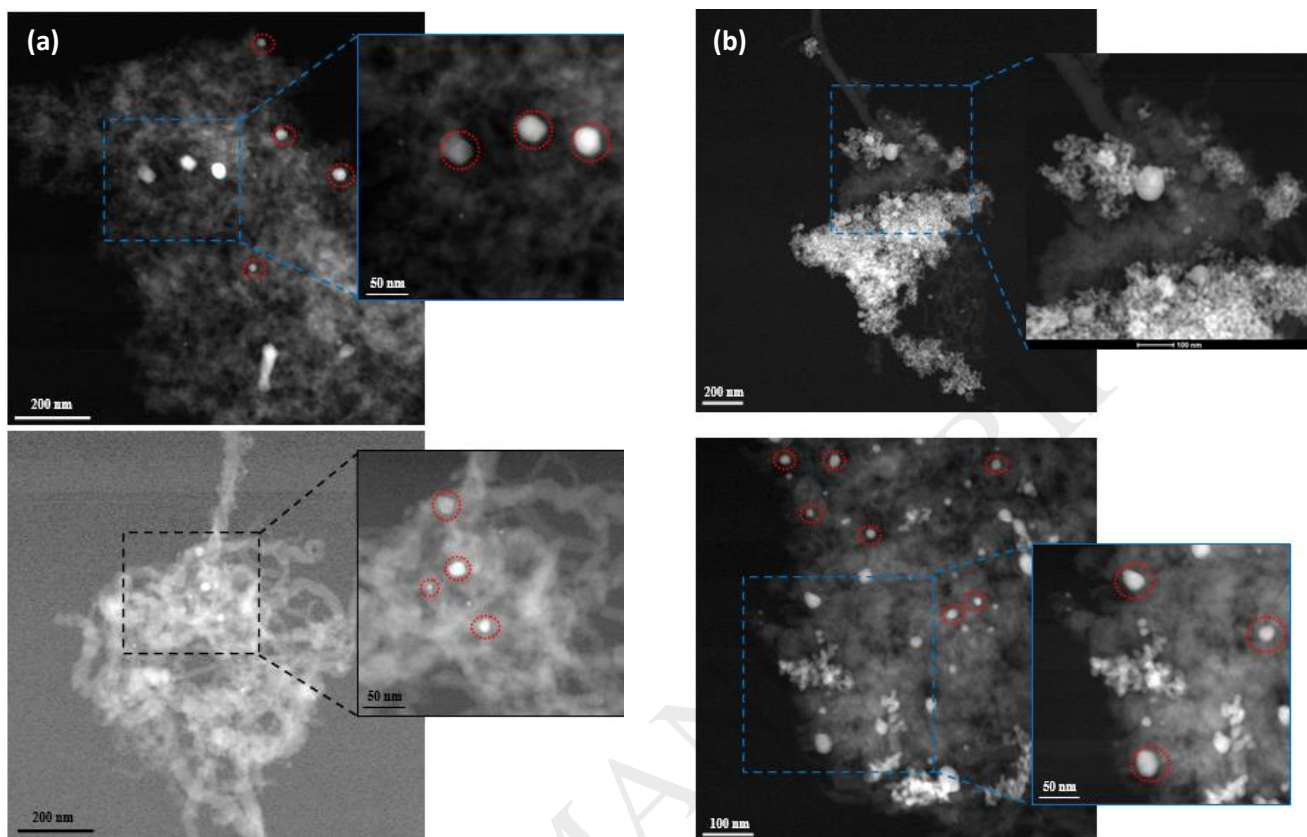


Fig 11.

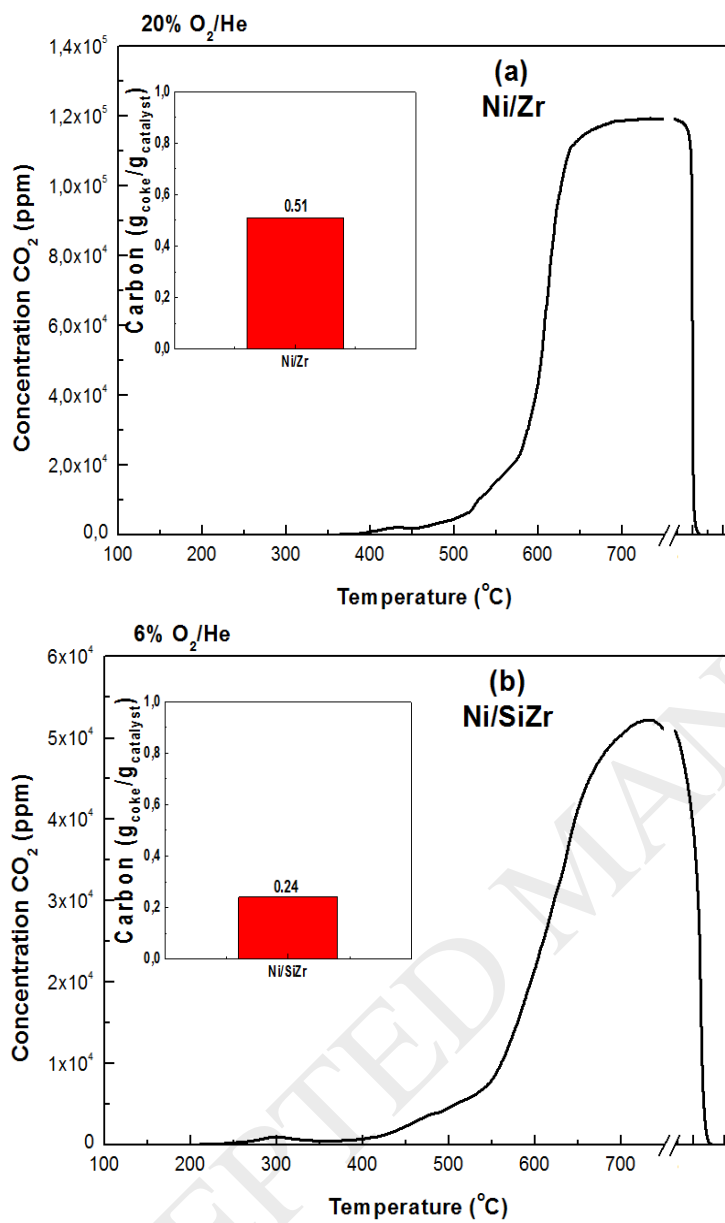


Fig 12.

## Tables

**Table 1.** Properties of untreated catalyst carriers

<b>Support</b>	<b>ZrO<sub>2</sub></b>	<b>SiO<sub>2</sub>-ZrO<sub>2</sub></b>
Pellet size	3.0 mm	3.0 mm
Packing density, kg/m <sup>3</sup>	<i>n/a</i>	1179.9
Median pore diameter, nm	<i>n/a</i>	13.4
SSA, m <sup>2</sup> /g	77	81.8
V <sub>p</sub> , ml/g	0.30	0.33
ZrO <sub>2</sub>		92.0
HfO <sub>2</sub>		1.6
Al <sub>2</sub> O <sub>3</sub>		0.2
SiO <sub>2</sub>		5.0
TiO <sub>2</sub>		0.2
Fe <sub>2</sub> O <sub>3</sub>		0.1
Zirconium's Phase	Monoclinic	Monoclinic

*Note: n/a = not available*

**Table 2.** Physicochemical, structural and textural properties of calcined and reduced catalysts

Catalyst	Calcined samples				Reduced samples				
	Metal loading (Ni, wt. %)	SSA ( $m^2g^{-1}$ )	NiO mean crystallite size (nm) <sup>1</sup>	NiO dispersion (%) <sup>2</sup>	SSA ( $m^2g^{-1}$ )	Pore volume ( $cm^3/g$ )	Av. pore width (nm)	Ni <sup>0</sup> mean crystallite size (nm) <sup>1</sup>	Ni <sup>0</sup> dispersion (%) <sup>2</sup>
Ni/Zr	7.65	50	15.7	4.2	44	0.05	19.9	23.0	2.9
Ni/SiZr	7.29	59	18.0	3.7	51	0.14	22.2	15.0	4.4

Note: <sup>1</sup>Calculated by XRD measurements (Scherrer analysis), <sup>2</sup>Calculated by the Vannice method

**Table 3.** Catalytic performance of the Ni/Zr and Ni/SiZr catalysts at 600 °C, during 20 hr of stability tests (1st and last measurement)

Reaction Metric	Ni/Zr		Ni/SiZr	
	1 <sup>st</sup> measure.	Last measure	1 <sup>st</sup> measure.	Last measure
X <sub>(C<sub>3</sub>H<sub>8</sub>O<sub>3</sub>)</sub> , %	80.25	64.90	83.10	68.16
X <sub>(C<sub>3</sub>H<sub>8</sub>O<sub>3</sub>)</sub> ,into gaseous products, %	44.88	38.60	48.59	37.89
Y <sub>(H<sub>2</sub>)</sub>	2.33	1.50	2.88	2.08
S <sub>(H<sub>2</sub>)</sub> , %	74.25	55.72	87.88	76.67
S <sub>(CO<sub>2</sub>)</sub> , %	50.89	39.48	67.94	57.67
S <sub>(CO)</sub> , %	45.44	52.31	30.05	39.98
S <sub>(CH<sub>4</sub>)</sub> , %	3.66	8.20	1.99	2.33
S <sub>(acetol)</sub> , %	43.37	39.96	45.27	40.48
S <sub>(acetone)</sub> , %	11.84	11.11	11.63	11.35
S <sub>(allyl alcohol)</sub> , %	19.65	22.96	18.55	23.58
S <sub>(acetaldehyde)</sub> , %	14.96	15.77	11.93	13.41
S <sub>(acetic acid)</sub> , %	10.17	10.19	12.62	11.18
H <sub>2</sub> /CO	3.81	2.48	6.82	4.59
CO/CO <sub>2</sub>	0.89	1.32	0.44	0.69